

# LLM-Based Scientific Equation Discovery via Physics-Informed Token-Regularized Policy Optimization

Boxiao Wang

wangboxiao22@mails.ucas.ac.cn  
Institute of Automation, Chinese  
Academy of Sciences  
Beijing, China

Chen Li

lichen@skla.cadrc.cn  
State Key Laboratory of  
Aerodynamics  
Mianyang, Sichuan, China

Kai Li\*

kai.li@ia.ac.cn  
Institute of Automation, Chinese  
Academy of Sciences  
Beijing, China

Junzhe Wang

wangjunzhe21@mails.ucas.ac.cn  
School of Mathematical Sciences,  
University of Chinese Academy of  
Sciences  
Beijing, China

Jian Cheng

jian.cheng@ia.ac.cn  
Institute of Automation, Chinese  
Academy of Sciences  
Beijing, China

Tianyi Liu

franktyliu@outlook.com  
State Key Laboratory of  
Aerodynamics  
Mianyang, Sichuan, China

Yifan Zhang

yifan.zhang@ia.ac.cn  
Institute of Automation, Chinese  
Academy of Sciences  
Beijing, China

## Abstract

Symbolic regression aims to distill mathematical equations from observational data. Recent approaches have successfully leveraged Large Language Models (LLMs) to generate equation hypotheses, capitalizing on their vast pre-trained scientific priors. However, existing frameworks predominantly treat the LLM as a static generator, relying on prompt-level guidance to steer exploration. This paradigm fails to update the model's internal representations based on search feedback, often yielding physically inconsistent or mathematically redundant expressions. In this work, we propose **PiT-PO** (Physics-informed Token-regularized Policy Optimization), a unified framework that evolves the LLM into an adaptive generator via reinforcement learning. Central to PiT-PO is a *dual-constraint mechanism* that rigorously enforces hierarchical physical validity while simultaneously applying fine-grained, token-level penalties to suppress redundant structures. Consequently, PiT-PO aligns LLM to produce equations that are both scientifically consistent and structurally parsimonious. Empirically, PiT-PO achieves state-of-the-art performance on standard benchmarks and successfully discovers novel turbulence models for challenging fluid dynamics problems. We also demonstrate that PiT-PO empowers small-scale models to outperform closed-source giants, democratizing access to high-performance scientific discovery.

## 1 Introduction

Symbolic Regression (SR) [22] stands as a cornerstone of data-driven scientific discovery, uniquely capable of distilling interpretable mathematical equations from observational data. Unlike black-box models that prioritize mere prediction, SR elucidates the fundamental mechanisms governing system behavior, proving instrumental in uncovering physical laws [21, 34], modeling chemical kinetics [4, 7], and analyzing complex biological dynamics [39, 48].

However, the search for exact governing equations represents a formidable challenge, formally classified as an NP-hard problem [47]. To navigate this vast search space, algorithmic strategies have evolved from Genetic Programming (GP) [5, 37] and Reinforcement Learning (RL) [31] to Transformer-based architectures that map numerical data directly to symbolic equations [2, 14, 53]. Most recently, the advent of Large Language Models (LLMs) has introduced a new paradigm. Methods such as LLM-SR [40] and LaSR [10] leverage the pre-trained scientific priors and in-context learning capabilities of LLMs to generate equation hypotheses. These approaches typically employ an evolutionary search paradigm, where candidates are evaluated, and high-performing solutions are fed back via prompt-level conditioning to steer subsequent generation.

Despite encouraging progress, existing LLM-based SR methods remain constrained by severe limitations. First, most approaches treat the LLM as a static generator, relying primarily on prompt-level, *verbal* guidance to steer the evolutionary search [10, 40]. This “frozen” paradigm inherently neglects the opportunity to adapt and enhance the generative capability of the LLM itself based on evaluation signals, preventing the model from internalizing feedback and adjusting its generation strategies to the specific problem. Second, they typically operate in a physics-agnostic manner, prioritizing syntactic correctness over physical validity [10, 40]. Without rigorous constraints, LLMs often generate equations that fit the data numerically but violate fundamental physical principles, rendering them prone to overfitting and practically unusable.

In this work, we propose to fundamentally shift the role of the LLM in SR from a static proposer to an adaptive generator. We establish a dynamic feedback loop in which evolutionary exploration and parametric learning reinforce each other: evolutionary search uncovers diverse candidate equations and generates informative evaluation signals, while parametric adaptation enables the LLM

to consolidate effective symbolic patterns and guide subsequent exploration more efficiently. By employing *in-search* fine-tuning, i.e., updating the LLM parameters during the evolutionary search process, we move beyond purely verbal, prompt-level guidance and introduce *numerical* guidance that allows feedback to be directly internalized into the model parameters, progressively aligning LLM with the intrinsic properties of the target system.

To realize this vision, we introduce PiT-PO (Physics-informed Token-regularized Policy Optimization), a unified framework that bridges LLM-driven evolutionary exploration with rigorous verification. PiT-PO is built upon two technical components. **1) In-Search LLM Evolution.** We implement the numerical guidance via reinforcement learning, which efficiently updates the LLM’s parameters during the search process. Instead of relying on static pre-trained knowledge, this in-search policy optimization enables LLM to dynamically align its generative distribution with the structural characteristics of the specific task, effectively transforming general scientific priors into domain-specific expertise on the fly. **2) Dual Constraints as Search Guidance.** We enforce hierarchical physical constraints to ensure scientific validity, and uniquely, we incorporate a fine-grained regularization based on our proposed *Support Exclusion Theorem*. This theorem allows us to identify mathematically redundant terms and translate them into token-level penalties, effectively pruning the search space and guiding LLM toward physically meaningful and structurally parsimonious equations.

Comprehensive experimental results demonstrate that PiT-PO achieves state-of-the-art performance across standard SR benchmarks, including the LLM-SR Suite [40] and LLM-SRBench [41], and recovers the largest number of ground-truth equations among all evaluated methods. In addition to synthetic benchmarks, the effectiveness of PiT-PO is validated on an application-driven turbulence modeling task involving flow over periodic hills. PiT-PO improves upon traditional Reynolds-Averaged Navier-Stokes (RANS) approaches by producing anisotropic Reynolds stresses closer to Direct Numerical Simulation (DNS) references. The learned method shows enhanced physical consistency, with reduced non-physical extremes and better flow field predictions. Finally, PiT-PO maintains robust performance even when using resource-constrained small models, such as a quantized version of Llama-8B, and remains efficient under strict wall-clock time budgets, establishing a practical methodology for automated scientific discovery.

## 2 Preliminaries

### 2.1 Problem Setup

In SR, a dataset of input–output observations is given:

$$D = \{(x_i, y_i)\}_{i=1}^n, \quad x_i \in \mathbb{R}^d, \quad y_i \in \mathbb{R}. \quad (1)$$

The objective is to identify a compact and interpretable function  $f \in \mathcal{F}$  such that  $f(x_i) \approx y_i$  for the observed samples, while retaining the ability to generalize to unseen inputs.

### 2.2 LLM-based SR Methods

Contemporary LLM-based approaches reformulate SR as a iterative program synthesis task. In this paradigm, typified by frameworks such as LLM-SR [40], the discovery process is decoupled into

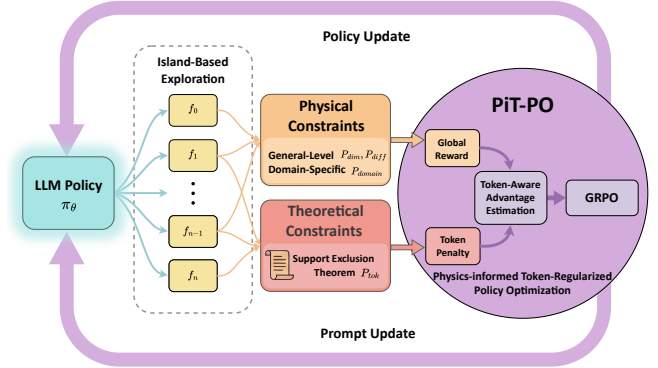


**Figure 1: The overall framework of PiT-PO.** PiT-PO transforms the LLM from a static proposer into an adaptive generator via a closed-loop evolutionary process. The framework integrates dual-constraint evaluation—comprising physical constraints and theoretical constraints—to generate fine-grained token-level learning signals. These signals guide the LLM policy update via reinforcement learning, ensuring the discovery of parsimonious, physically consistent equations.

two phases: structure proposal and parameter estimation. Specifically, the LLM functions as a symbolic generator, emitting functional skeletons with placeholders for learnable coefficients. A numerical optimizer (e.g., BFGS [9]) subsequently fits these constants to the observed data. To navigate the combinatorial search space, these methods employ an evolutionary-style feedback loop: high-fitness equations are maintained in a pool to serve as in-context examples, prompting the LLM to refine subsequent generations. Our work leverages this architecture as a backbone, but fundamentally redefines the LLM’s role from a static proposer to an adaptive generator.

### 2.3 Group Relative Policy Optimization

Group Relative Policy Optimization (GRPO) [38] is a RL algorithm tailored for optimizing LLMs on reasoning tasks, characterized by its efficient baseline estimation without the need for a separate value network. In the context of LLM-based SR, the generation process is modeled as a Markov Decision Process (MDP), where LLM functions as a policy  $\pi_\theta$  that generates a sequence of tokens  $o = (t_1, \dots, t_L)$  given a prompt  $q$ . For each  $q$ , GRPO samples a group of  $G$  outputs  $\{o_1, \dots, o_G\}$  from the sampling policy  $\pi_{\theta_{old}}$ . GRPO maximizes the following surrogate loss function:

$$\mathcal{L}_{GRPO}(\theta) = \mathbb{E}_{q \sim P(Q), \{o_i\} \sim \pi_{\theta_{old}}} \left[ \frac{1}{G} \sum_{i=1}^G \left( \frac{1}{L_i} \sum_{k=1}^{L_i} \mathcal{L}_{i,k}^{clip}(\theta) - \beta \mathbb{D}_{KL}(\pi_\theta || \pi_{ref}) \right) \right], \quad (2)$$

where  $\pi_{ref}$  is the reference policy to prevent excessive deviation, and  $\beta$  controls the KL-divergence penalty. The clipping term  $\mathcal{L}_{i,k}^{clip}(\theta)$  ensures trust region updates:

$$\mathcal{L}_{i,k}^{clip}(\theta) = \min \left( \frac{\pi_\theta(t_{i,k}|q, o_{i,<k})}{\pi_{\theta_{old}}(t_{i,k}|q, o_{i,<k})} \hat{A}_i, \text{clip} \left( \frac{\pi_\theta(t_{i,k}|q, o_{i,<k})}{\pi_{\theta_{old}}(t_{i,k}|q, o_{i,<k})}, 1 - \epsilon, 1 + \epsilon \right) \hat{A}_i \right). \quad (3)$$

Here,  $\epsilon$  is the clipping coefficient. A distinctive feature of GRPO lies in its advantage estimation, it computes the advantage  $\hat{A}_i$  by

standardizing the reward  $R(o_i)$  relative to the group:

$$\hat{A}_i = \frac{R(o_i) - \text{mean}(\{R(o_j)\})}{\text{std}(\{R(o_j)\})}. \quad (4)$$

Consequently, every token within the sequence  $o_i$  is assigned the exact same feedback signal. This coarse granularity treats valid and redundant terms indistinguishably, a limitation that our work addresses by introducing fine-grained, token-level regularization.

### 3 Method

We propose PiT-PO (Physics-informed Token-regularized Policy Optimization), a framework that evolves LLM into an adaptive, physics-aware generator. PiT-PO establishes a closed-loop evolutionary process driven by two synergistic mechanisms: (1) a dual-constraint evaluation system that rigorously assesses candidates through hierarchical physical verification and theorem-guided redundancy pruning; and (2) a novel policy optimization strategy that updates LLM using fine-grained, token-level feedback derived from these constraints. This combination effectively aligns the LLM with the intrinsic structure of the problem, guiding the LLM toward solutions that are not only numerically accurate but also structurally parsimonious and scientifically consistent.

#### 3.1 Dual-Constraint Learning Signals

Navigating the combinatorial space of symbolic equations requires rigorous guidance. We employ a reward system driven by dual constraints: physical constraints delineate the scientifically valid region, while theoretical constraints drive the search toward simpler equations by identifying and pruning redundant terms.

**3.1.1 Hierarchical Physical Constraints.** To ensure scientific validity, we construct a hierarchical filter that categorizes constraints into two levels: general properties and domain-specific priors.

**General-Level Constraints.** We enforce fundamental physical properties applicable across scientific disciplines. To prune physically impossible structures (e.g., adding terms with mismatched units), we assign penalty-based rewards for Dimensional Homogeneity ( $P_{\text{dim}}$ ) and Differentiability ( $P_{\text{diff}}$ ). The former strictly penalizes equations with unit inconsistencies, while the latter enforces smoothness on the data-defined domain.

**Domain-Specific Constraints.** To tackle specialized tasks, we inject expert knowledge as inductive biases. We define the domain-specific penalty  $P_{\text{domain}}^{(j)}$  to penalize candidate equations that violate the  $j$ -th domain-specific constraint. Taking the turbulence modeling task (detailed in Appendix E.4) as a representative instantiation, we enforce four rigorous constraints: (1) Realizability [32], ensuring the Reynolds stress tensor has positive eigenvalues; (2) Boundary Condition Consistency [27], requiring stresses to decay to zero at the wall; (3) Asymptotic Scaling [44, 49], enforcing the cubic relationship between stress and wall distance in the viscous sublayer; and (4) Energy Consistency [26, 32], aligning predicted stress with turbulent kinetic energy production.

This hierarchical design effectively embeds physical consistency as a hard constraint in the reward function, prioritizing scientific validity over mere empirical fitting.

**3.1.2 Theorem-Guided Mathematical Constraints.** While physical constraints ensure validity, they do not prevent mathematical redundancy. To rigorously distinguish between essential terms and redundant artifacts, we introduce the Support Exclusion Theorem.

Let  $\mathcal{S}$  denote the **full support set** containing all candidate basis functions  $\{\phi_j\}$ . The **ground truth equation** is  $f^* = \sum_{j \in \mathcal{S}'} a_j \phi_j$ , where  $\mathcal{S}' \subseteq \mathcal{S}$  is the **true support set** (i.e., the indices of basis functions that truly appear in the governing equation), and  $\{a_j\}_{j \in \mathcal{S}'}$  are the corresponding true coefficients. Consider a candidate equation  $f = \sum_{j \in \mathcal{K}} b_j \phi_j$ , where  $\mathcal{K} \subseteq \mathcal{S}$  represents the **current support set** (i.e., the selected terms in the skeleton),  $\mathbf{b} = \{b_j\}_{j \in \mathcal{K}}$  are the optimized coefficients derived from the data. We define the empirical Gram matrix of these basis functions as  $G \in \mathbb{R}^{|\mathcal{S}| \times |\mathcal{S}|}$  and the corresponding Projection Matrix as  $T$ , where  $T_{ij} := G_{ji} / G_{ii}$ .

**THEOREM 3.1 (SUPPORT EXCLUSION THEOREM).** *Assume the ground-truth support is finite and satisfies  $|\mathcal{S}'| \leq M$ , and let the true function coefficients be bounded by  $A \leq |a_j| \leq B$  for all  $j \in \mathcal{S}'$ . A term  $\phi_i$  ( $i \in \mathcal{K}$ ) is theoretically guaranteed to be a false discovery (not in the true support  $\mathcal{S}'$ ) if its fitted coefficient magnitude satisfies:*

$$|b_i| < A - \left( \underbrace{\sum_{j \in \mathcal{K}, j \neq i} (B + |b_j|) |T_{ij}|}_{\text{Internal Interference}} + \underbrace{B \sum_{k=1}^m s(k)}_{\text{External Interference}} \right). \quad (5)$$

$s(k)$  denotes the  $k$ -th largest value in  $\{|T_{i\ell}| : \ell \in \mathcal{S} \setminus \mathcal{K}\}$ , and  $m := \min(M - 1, |\mathcal{S} \setminus \mathcal{K}|)$ .

Detailed definitions of all notations and the rigorous proof of Theorem 3.1 are provided in Appendix B. This theorem formalizes the intuition that coefficients of redundant terms (absent from the true support  $\mathcal{S}'$ ) have significantly smaller magnitudes than those of valid components.

Specifically, after fitting  $\mathbf{b}$ , we compute the normalized coefficient ratio  $\tau_i = |b_i| / (\sum_j |b_j| + \epsilon)$ . We introduce a threshold  $\rho \in (0, 1)$  to identify potentially redundant terms. Terms satisfying  $\tau_i > \rho$  incur no penalty, while components with  $\tau_i \leq \rho$  are considered redundant. To suppress these redundancies, we define a **token penalty** for each token in redundant term  $i$ :

$$P_{\text{tok}} = p \cdot \max(0, -\log(|b_i| + \epsilon)), \quad (6)$$

where  $p > 0$  is a scaling coefficient. We use a logarithmic scale to impose stronger penalties on terms with smaller coefficients.

By integrating this penalty into the policy optimization, we guide the LLM to reduce the probability of generating redundant terms, thereby steering the optimization toward parsimonious equations.

#### 3.2 Token-Aware Policy Update

Our proposed PiT-PO effectively operationalize the hierarchical constraints and theoretical insights derived in Section 3.1. Unlike standard GRPO that assign a uniform scalar reward to the entire generated sequence, our method transitions the learning process from coarse-grained sequence scoring to fine-grained token-level credit assignment. This ensures that the policy not only learns to generate physically valid equations but also explicitly suppresses theoretically redundant terms.

**3.2.1 Global Reward with Gated Constraints.** The optimization is driven by a composite global reward,  $R_{global}$ , which balances fitting accuracy, structural parsimony, and physical consistency. Formally, for a sampled equation  $o_i$ , the rewards are defined as follows:

**Fitting Accuracy** ( $R_{fit}$ ). We use the normalized log-MSE to encourage precise data fitting:

$$R_{fit} = -\alpha \log(\text{MSE} + \epsilon), \quad (7)$$

where  $\text{MSE} = \frac{1}{n} \sum_{i=1}^n (y_i - \hat{y}_i)^2$ .

**Complexity Penalty** ( $P_{cplx}$ ). Adhering to Occam’s Razor, we penalize structural complexity based on the Abstract Syntax Tree (AST) [30] node count:

$$P_{cplx} = \lambda_{len} \cdot \text{Length}(\text{AST}). \quad (8)$$

In PiT-PO, each equation generated by the LLM is represented as a Python function and parsed into an AST, where each node corresponds to a variable or operator. The total node count provides a meaningful estimate of structural complexity.

**Gated Physical Penalty** ( $P_{phy}$ ). Imposing strict physical constraints too early can hinder exploration, causing the model to discard potentially promising functional forms. We therefore activate physical penalties only after the candidate equation reaches a baseline fitting accuracy threshold ( $\delta_{gate}$ ). Specifically, we define

$$P_{phy}(o_i) = \mathbb{1}(\text{MSE}(o_i) < \delta_{gate}) \left( P_{diff}(o_i) + P_{dim}(o_i) + \sum_{j=1}^J P_{\text{domain}}^{(j)}(o_i) \right), \quad (9)$$

where  $\mathbb{1}(\cdot)$  is the indicator function. This mechanism effectively creates a soft curriculum: it allows “free” exploration in the early stages and enforcing strict physical compliance only after the solution enters a plausible region.

The total reward  $R_{global}$  is then formulated as:

$$R_{global}(o_i) = R_{fit}(o_i) - P_{cplx}(o_i) - P_{phy}(o_i). \quad (10)$$

**3.2.2 Fine-Grained Advantage Estimation.** Standard GRPO applies a uniform advantage across all tokens in a sequence. We refine this by synthesizing the global reward with the token-level penalty  $P_{tok}$  (Equation 6). Specifically, we define the **token-aware advantage**  $\hat{A}_{i,k}$  for the  $k$ -th token in the  $i$ -th sampled equation as:

$$\hat{A}_{i,k} = \frac{R_{global}(o_i) - \mu_{group}}{\sigma_{group}} - \underbrace{\frac{P_{i,k}}{\widetilde{P}_{i,k}}}_{\text{Local Pruning}}. \quad (11)$$

Here, the first term standardizes the global reward against the group statistics ( $\mu_{group}, \sigma_{group}$ ), reinforcing equations that satisfy multi-objective criteria relative to their peers. The second term,  $P_{i,k}$ , applies a targeted penalty to suppress redundancy. Specifically, we set  $P_{i,k} = 0$  if token  $k$  belongs to a non-redundant term, and  $P_{i,k} = P_{tok}$  otherwise. This ensures that penalties are applied exclusively to tokens contributing to mathematically redundant structures, while valid terms remain unaffected.

Substituting this token-aware advantage into the GRPO objective, the policy gradient update of our PiT-PO becomes:

$$\nabla \mathcal{J}_{\text{PiT-PO}} \propto \sum_{i,k} \hat{A}_{i,k} \nabla \log \pi_{\theta}(t_{i,k} | o_{i,<k}). \quad (12)$$

---

**Algorithm 1:** PiT-PO Overall Training Pipeline

---

```

Input: Dataset  $D = \{(x_i, y_i)\}_{i=1}^n$ ; LLM  $\pi_{\theta}$ ; number of islands  $N$ ; group size  $G$ ; iterations  $T$ .
Output: Best equation  $o^*$ .
1 Initialize  $o^*$ ,  $s^*$ , and buffers  $\mathcal{B}_j \leftarrow \emptyset$  for  $j = 1, \dots, N$ 
2 for  $t \leftarrow 1$  to  $T$  do
   // Stage 1: Island-Based Exploration
   3   for  $j \leftarrow 1$  to  $N$  do
      4      $q_j \leftarrow \text{BUILD_PROMPT}(D, \mathcal{B}_j)$  // in-context rule
      5      $\{o_i\}_{i=1}^G \sim \pi_{\theta}(\cdot | q_j)$  // sample a group
      6     for  $i \leftarrow 1$  to  $G$  do
         7        $(R_i, \{P_{i,k}\}) \leftarrow \text{DUALCONSTRAINTEVAL}(o_i, D)$ 
         8       //  $R_i = R_{global}(o_i)$ 
         9        $\mathcal{B}_j \leftarrow \mathcal{B}_j \cup \{(q_j, o_i, R_i, \{P_{i,k}\})\}$ 
        10      if  $R_i > s^*$  then
           11         $o^* \leftarrow o_i$ ;  $s^* \leftarrow R_i$ 
   // Stage 2: In-Search LLM Evolution
   12    $\theta \leftarrow \text{PiT-PO\_UPDATE}(\theta, \{\mathcal{B}_j\}_{j=1}^N, \pi_{\theta})$ 
   // Stage 3: Hierarchical Selection
   13    $\{\mathcal{B}_j\}_{j=1}^N \leftarrow \text{SELECTANDRESET}(\{\mathcal{B}_j\}_{j=1}^N)$ 
13 return  $o^*$ 

```

---

This creates a dual-pressure optimization landscape: global rewards guide the policy toward physically consistent and accurate equations, while local penalties surgically excise redundant terms. This ensures the final output aligns with the sparse, underlying physical laws rather than merely overfitting numerical data.

### 3.3 Overall Training Pipeline

We orchestrate the PiT-PO framework through a closed-loop evolutionary RL cycle. As illustrated in Algorithm 1, the training process iterates through three synergistic phases:

**Phase 1: Island-Based Exploration (Data Generation).** To prevent premature convergence to local optima, a common pitfall in SR, we employ a standard multi-island topology ( $N$  islands) to structurally enforce search diversity [5, 35]. Each island  $j$  maintains an isolated experience buffer  $\mathcal{B}_j$ , evolving its own lineage of equations. This information isolation allows distinct islands to cultivate diverse functional forms independently.

**Phase 2: In-Search LLM Evolution (Policy Update).** This phase transforms the collected data into parametric knowledge. We aggregate the trajectories from all  $N$  islands into a global batch to perform policy optimization using PiT-PO. By minimizing the loss, the model explicitly lowers the probability of generating mathematically redundant tokens and physically inconsistent structures. To ensure computational efficiency during this iterative search, we implement the update using Low-Rank Adaptation (LoRA) [12].

**Phase 3: Hierarchical Selection (Population Management).** We apply standard survival-of-the-fittest mechanisms to maintain population quality. Local buffers  $\mathcal{B}_j$  are updated by retaining only top-performing candidates, while underperforming islands are periodically reset with high-fitness seeds to escape local optima.

This cycle establishes a reciprocal reinforcement mechanism: the island-based exploration maintains search diversity, while policy update consolidates these findings into the model weights, progressively transforming the LLM into a domain-specialized scientific discoverer.

## 4 Experiments

### 4.1 Setup

**Benchmarks.** To provide a comprehensive evaluation of PiT-PO, we adopt two widely used benchmarks to compare against state-of-the-art baselines:

*LLM-SR Suite* [40]. This suite comprises four tasks spanning multiple scientific domains: *Oscillation 1 & 2* (Nonlinear Oscillatory Systems) feature dissipative couplings and non-polynomial nonlinearities with explicit forcing, making recovery of the correct interaction terms from trajectory data non-trivial; *E. coli Growth* [28, 36] models multivariate population dynamics with strongly coupled, multiplicative effects from nutrients, temperature, and acidity; and *Stress-Strain* [1] uses experimental measurements of Aluminum 6061-T651 and exhibits temperature-dependent, piecewise non-linear deformation behavior. Detailed information about these tasks is provided in Appendix D.1.

*LLM-SRBench*: [41] To evaluate generalization beyond canonical forms, we adopt the comprehensive LLM-SRBench benchmark, which contains 239 tasks organized into two complementary subsets, LSR-Transform and LSR-Synth. LSR-Transform changes the prediction target to rewrite well-known physics equations into less common yet analytically equivalent forms, producing 111 transformed tasks. This design aims to reduce reliance on direct memorization of canonical templates and tests whether a method can recover the same physical law under non-trivial variable reparameterizations. Complementarily, LSR-Synth composes equations from both known scientific terms and synthetic but plausible terms to further assess discovery beyond memorized templates: candidate terms are proposed by an LLM under domain context, assembled into full equations, and then filtered through multiple checks, including numerical solvability, contextual novelty, and expert plausibility, yielding 128 synthetic tasks. Further details are given in Appendix D.2.

### Baselines.

We compare PiT-PO against representative baselines spanning both classical and LLM-based SR methods. For the four tasks in the LLM-SR Suite, we include GPlearn, a genetic programming-based SR approach; PySR [10], which couples evolutionary search with symbolic simplification; uDSR [17], which replaces the RNN policy in DSR with a pretrained Transformer and employs neural-guided decoding; RAG-SR [53], which incorporates structure retrieval to assist equation generation; and LLM-SR [40]. For the broader LLM-SRBench benchmark, we further compare against leading LLM-based SR methods, including SGA [20], which integrates LLM-driven hypothesis proposal with physics-informed parameter optimization in a bilevel search framework, and LaSR [10], which leverages abstract symbolic concepts distilled from prior equations to guide hybrid LLM-evolutionary generation.

**Evaluation metrics.** We evaluate methods using Accuracy to Tolerance and Normalized Mean Squared Error (NMSE). For a tolerance  $\tau$ , we report  $\text{Acc}_{\text{all}}(\tau)$  [2] and  $\text{Acc}_{\text{avg}}(\tau)$  based on relative error:  $\text{Acc}_{\text{all}}(\tau) = \mathbb{1}(\max_{1 \leq i \leq N_{\text{test}}} |\frac{\hat{y}_i - y_i}{y_i}| \leq \tau)$  and  $\text{Acc}_{\text{avg}}(\tau) = \frac{1}{N_{\text{test}}} \sum_{i=1}^{N_{\text{test}}} \mathbb{1}(|\frac{\hat{y}_i - y_i}{y_i}| \leq \tau)$ , where  $\hat{y}_i$  and  $y_i$  denote the predicted and ground-truth values at the  $i$ -th test point, respectively. We additionally report  $\text{NMSE} = \frac{1}{N_{\text{test}}} \sum_{i=1}^{N_{\text{test}}} \frac{(\hat{y}_i - y_i)^2}{\text{Var}(y)}$  to assess overall numerical accuracy. We additionally adopt the Symbolic Accuracy (SA) metric [41], which directly measures whether the discovered equation recovers the correct symbolic form (i.e., whether it is mathematically equivalent to the ground-truth equation up to fitted constants).

**Hyperparameter Configurations.** All experiments were run for 2,500 search iterations. To ensure a fair comparison, all hyperparameters related to LLM generation and search were kept consistent with the default configuration of LLM-SR. For the in-search policy optimization specific to PiT-PO, we use a learning rate of  $1 \times 10^{-6}$ , a group size of  $G = 4$ , and a multi-island setting of  $N = 4$ , resulting in an effective per-device batch size of  $G \times N = 16$ . The coefficient of the KL regularization term was set to 0.01, and the LoRA rank was set to  $r = 16$ . In addition, experiments were conducted on a single NVIDIA RTX 3090 using 4-bit quantized Llama-3.2-1B-Instruct, Llama-3.2-3B-Instruct, and Llama-3.1-8B-Instruct [15] to evaluate the training stability and performance transferability of PiT-PO across different parameter scales under constrained compute and memory budgets. More details are in Appendix A.

### 4.2 PiT-PO Demonstrates Superior Equation Discovery Capability

As evidenced in Table 1, PiT-PO establishes a new state-of-the-art on LLM-SR Suite. It consistently dominates baseline methods across all metrics, achieving the highest accuracy while maintaining the lowest NMSE in nearly all test cases. Crucially, when controlling for the LLM backbone, PiT-PO yields a substantial performance margin over LLM-SR, validating the effectiveness of our in-search policy optimization framework. Notably, PiT-PO is the only approach to successfully identify the exact ground-truth equation for the Oscillator 1. This structural precision extends to the larger-scale LLM-SRBench (Table 2), where PiT-PO achieves the highest symbolic accuracy across all categories. These results collectively demonstrate that PiT-PO not only fits data numerically but excels in uncovering the true underlying equations.

These quantitative gains are not accidental but stem from PiT-PO’s structural awareness. Analysis of the iterative trajectories of LLM-SR and PiT-PO in Appendix C.4 corroborates this conclusion: the iterations of LLM-SR remain persistently influenced by clearly incorrect terms, which violate physical meaning despite providing strong numerical fits, as well as by additional nuisance terms. Consequently, the search of LLM-SR often stagnates in a low-MSE regime without reaching the correct structure. In contrast, once PiT-PO enters the same regime, the dual constraints rapidly eliminate terms that improve fitting performance but are structurally incorrect. This behavior highlights the central advantage of the proposed dual-constraint learning signals, in which the physical constraints and token-level penalties provide data-driven signals

Models	Oscillation 1		Oscillation 2		E. coli growth		Stress-Strain	
	Acc <sub>avg-0.001(%)↑</sub>	NMSE↓	Acc <sub>avg-0.001(%)↑</sub>	NMSE↓	Acc <sub>avg-0.1(%)↑</sub>	NMSE↓	Acc <sub>avg-0.1(%)↑</sub>	NMSE↓
GPtern	0.11	0.0972	0.05	0.2000	0.76	1.0023	28.43	0.3496
uDSR	1.78	0.0002	0.36	0.0856	1.12	0.5059	59.15	0.0639
PySR	3.80	0.0003	7.02	0.0002	2.80	0.4068	70.60	0.0347
RAG-SR	39.47	1.49e-6	0.43	0.0282	2.04	0.2754	76.28	0.0282
LLM-SR (Mixtral)	<b>100.00</b>	1.32e-11	99.98	1.18e-11	2.88	0.0596	71.44	0.0276
LLM-SR (4o-mini)	99.92	8.84e-12	99.97	8.70e-10	5.52	0.0453	<b>85.33</b>	0.0245
LLM-SR (Llama-3.1-8B)	59.58	1.17e-6	99.96	9.66e-10	4.86	0.0555	77.74	0.0246
LLM-SR (Llama-3.2-3B)	39.45	1.76e-6	66.34	6.99e-7	1.08	0.3671	74.78	0.0324
LLM-SR (Llama-3.2-1B)	3.28	4.47e-4	7.81	0.0002	1.70	0.5801	30.35	0.3801
PiT-PO (Llama-3.1-8B)	<b>100.00</b>	<b>6.41e-31</b>	<b>99.99</b>	<b>2.11e-13</b>	<b>10.42</b>	<b>0.0090</b>	84.45	<b>0.0136</b>
PiT-PO (Llama-3.2-3B)	<b>100.00</b>	<b>7.58e-31</b>	99.97	9.77e-10	7.01	0.0248	84.54	0.0156
PiT-PO (Llama-3.2-1B)	99.95	1.34e-11	99.97	1.70e-8	4.76	0.0240	76.91	0.1767

Table 1: Overall performance on LLM-SR Suite.

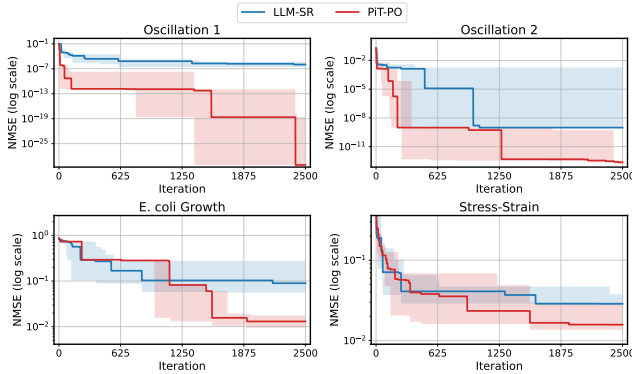


Figure 2: NMSE trajectories (log scale) over search iterations for LLM-SR and PiT-PO (Llama-3.1-8B) on LLM-SR Suite. Lines denote the median over seeds, and shaded regions indicate the min–max range. The remaining iteration curves for smaller backbones (3B and 1B) are deferred to Appendix C.1.

for precise structural correction, guiding the LLM toward the true underlying equation rather than mere numerical overfitting.

#### 4.3 PiT-PO Empowers Lightweight Backbones to Rival Large Models

As shown in Table 1, the performance of PiT-PO with the Llama-3.1-8B, Llama-3.2-3B, and Llama-3.2-1B backbones is competitive with, and often exceeds, the performance of LLM-SR that relies on substantially larger or proprietary models, including Mixtral 8×7B and 4o-mini.

These results indicate that PiT-PO effectively bridges the capability gap between lightweight open-source models and large-scale commercial systems. From a practical standpoint, this reduces the barrier to entry for scientific discovery: by delivering state-of-the-art performance on consumer-grade hardware (even maintaining competitiveness with a 1B backbone), PiT-PO eliminates the dependence on massive compute and closed-source APIs, thereby democratizing access to powerful SR tools.

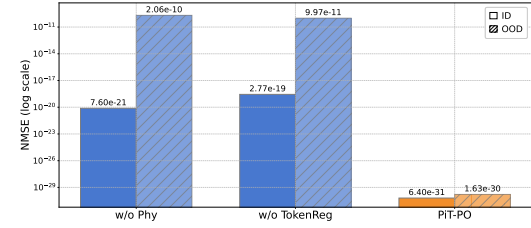


Figure 3: Ablation results of PiT-PO and its variants.

#### 4.4 PiT-PO Enhances Search Efficiency and Breaks Stagnation

Figure 2 shows that PiT-PO achieves superior search efficiency in discovering accurate equations. In the early search stage, the red and blue curves are close across all four tasks: both methods primarily rely on the fitting signal (MSE) and therefore exhibit comparable per-iteration progress. As NMSE enters a lower regime, the trajectories consistently separate: PiT-PO exhibits abrupt step-wise drops while LLM-SR tends to plateau, yielding a clear red-blue gap in every subplot. Concretely, once the search reaches these lower-error regions, PiT-PO repeatedly exits stagnation and transitions to the next accuracy phase with orders-of-magnitude NMSE reductions (most prominently in Oscillation 1 and Oscillation 2, and also evident in E. coli Growth and Stress-Strain), whereas LLM-SR often remains trapped near its current error floor. This behavior confirms that the proposed dual-constraint mechanism effectively activates exactly when naive MSE feedback becomes insufficient. By penalizing physical inconsistencies and structural redundancy, PiT-PO forces the LLM to exit stagnation and transition toward the correct functional form.

While the in-search fine-tuning introduces a computational overhead, this cost is decisively outweighed by the substantial gains in performance. As detailed in Appendix C.2, PiT-PO maintains a significant performance edge even when evaluated under equivalent wall-clock time, demonstrating that the accelerated convergence speed effectively compensates for the additional training time.

Models	LSR-Transform						LSR-Synth					
	Chemistry			Biology			Physics			Material Science		
	SA(%)↑	Acc <sub>all-0.1</sub> (%)↑	NMSE↓	SA(%)↑	Acc <sub>all-0.1</sub> (%)↑	NMSE↓	SA(%)↑	Acc <sub>all-0.1</sub> (%)↑	NMSE↓	SA(%)↑	Acc <sub>all-0.1</sub> (%)↑	NMSE↓
Direct Prompting	3.61	1.801	0.3697	0.00	0.00	0.0644	0.00	0.00	0.5481	0.00	0.00	0.0459
SGA	2.70	0.909	0.3519	0.00	8.33	0.0458	0.00	0.00	0.2416	0.00	2.27	0.1549
LaSR	5.41	45.94	<b>0.0021</b>	0.00	27.77	2.77e-4	4.16	16.66	2.73e-4	4.54	25.02	0.0018
LLM-SR	30.63	38.55	0.0101	8.33	66.66	8.01e-6	25.30	58.33	1.04e-6	6.97	34.09	1.23e-4
PiT-PO	<b>34.23</b>	<b>46.84</b>	0.0056	<b>13.89</b>	<b>77.78</b>	<b>4.13e-7</b>	<b>29.17</b>	<b>70.83</b>	<b>9.37e-8</b>	<b>11.36</b>	<b>40.91</b>	<b>6.57e-5</b>
											<b>12.00</b>	<b>92.00</b>
												<b>1.18e-8</b>

Table 2: Overall performance on LLM-SRBench (Llama-3.1-8B-Instruct).

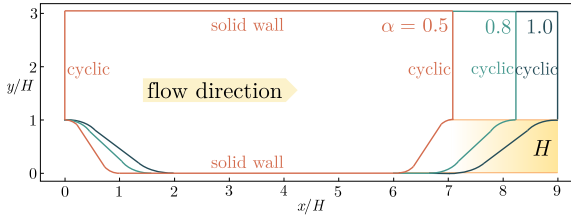


Figure 4: Schematic of the geometries for periodic hills.

## 4.5 Ablation Study

To rigorously validate the contribution of each algorithmic component, we conduct an ablation study across three settings: **w/o Phy**, which excludes the physics-consistency penalty  $P_{\text{phy}}$ ; **w/o Token-Reg**, which removes the redundancy-aware token-level regularization; and the full **PiT-PO** framework. As shown in Figure 3, removing any single component leads to a substantial deterioration of NMSE and a larger generalization gap between In-Distribution (ID) and Out-Of-Distribution (OOD) data. These empirical results underscore the necessity of the complete framework, demonstrating that the proposed dual constraints are indispensable for ensuring both search stability and robust generalization.

## 4.6 Case Study: Turbulence Modeling

To validate the practical utility of PiT-PO in high-fidelity scientific discovery, we select the **Flow over Periodic Hills** [52] (Figure 4) as a testbed. This problem is widely recognized in Computational Fluid Dynamics (CFD) [32] as a benchmark for *Separated Turbulent Flows*, presenting complex features such as strong adverse pressure gradients, massive flow detachment, and reattachment.

**Problem Definition and Physics:** The geometry consists of a sequence of polynomially shaped hills arranged periodically in the streamwise direction. The flow is driven by a constant body force at a bulk Reynolds number of  $Re_b = 5600$  (based on hill height  $H$  and bulk velocity  $U_b$ ). The domain height is fixed at  $L_y/H = 3.036$ , while the streamwise length  $L_x$  varies with the slope factor  $\alpha$  according to  $L_x/H = 3.858\alpha + 5.142$ . Periodic boundary conditions are applied in the streamwise direction, with no-slip conditions on the walls.

**The Scientific Challenge:** The challenge lies in the **Separation Bubble** [32], a region where turbulence exhibits strong **anisotropy** due to streamline curvature. Traditional Linear Eddy Viscosity Models (LEVM) [32], such as the  $k-\omega$  SST model [23, 24], rely on the

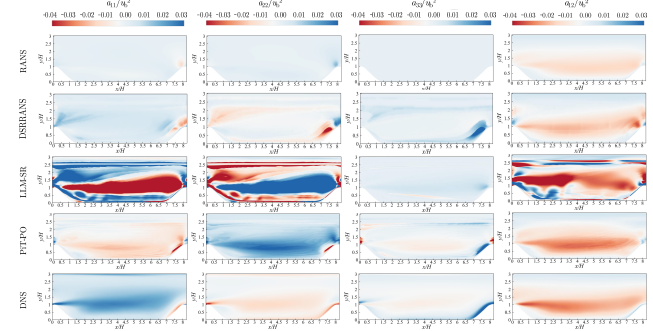


Figure 5: Comparison of the four anisotropic Reynolds stress components for periodic hill training flow using RANS, DSRRANS, LLM-SR, PiT-PO and DNS, respectively.

Boussinesq hypothesis which assumes isotropic turbulence. Consequently, they systematically fail to predict key flow features, such as the separation bubble size and reattachment location.

**Discovery Objective:** Instead of fitting a simple curve, our goal is to discover a **Non-linear Constitutive Relation** for the Reynolds stress anisotropy tensor  $a_{ij}$  and the dimensionless Reynolds stress anisotropy tensor  $b_{ij}$ . By learning the Reynolds stress tensor  $\tau_{ij}$  from high-fidelity Direct Numerical Simulation (DNS) [32] data, PiT-PO aims to formulate a symbolic correction term that captures the anisotropic physics missed by linear models.

**Baselines:** We follow standard turbulence modeling protocols and compare primarily against the standard  $k-\omega$  SST model of RANS. We also include LLM-SR and DSRRANS [42], a strong SR-based turbulence modeling method specifically designed for turbulence tasks.

We cast turbulence closure modeling as a SR problem [43] (see Appendix E for details). After obtaining the final symbolic equation, we embed it into a RANS solver of OpenFOAM [50] and run CFD simulations on the periodic-hill configuration. We compare the resulting Reynolds-stress components, mean-velocity fields, and skin-friction profiles against DNS references. Figures 5–7 visualize these quantities, enabling a direct assessment of physical fidelity and flow-field prediction quality.

Based on the comparative analysis of the anisotropic Reynolds stress contours (Figure 5), DSRRANS and PiT-PO show enhancement over the traditional RANS approach. Among them, PiT-PO performs the best: its contour matches the DNS reference most closely, with reduced error compared to DSRRANS and LLM-SR, demonstrating less severe non-physical extremes.

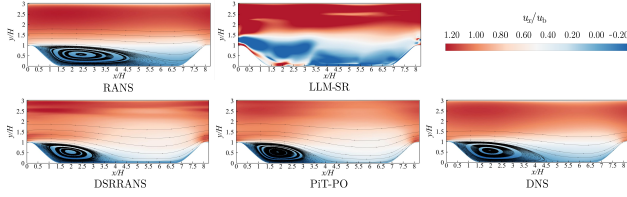


**Figure 6: Non-dimensional stream-wise velocity contours obtained by the learned model and the standard  $k-\omega$  SST model of RANS, compared with DNS data.**

The stream-wise velocity contours illustrate the correction of the bubble size, a region of reversed flow that forms when fluid detaches from a surface. In Figure 6, PiT-PO most accurately represents the extent and shape of the recirculation zone, where fluid circulates within the separated region, closely consistent with the DNS data throughout the domain, particularly within the separation region and the recovery layer, where flow re-attaches to the surface.

The skin friction coefficient (Figure 7), defined as the ratio of the wall stress to the dynamic pressure of the flow along the bottom wall, is a sensitive metric for predicting flow separation. The  $k-\omega$  SST model of RANS underestimates the magnitude of the skin friction and predicts a delayed reattachment location compared to the DNS. The learned model (PiT-PO) improves the prediction, aligning more closely with the DNS profile.

These results demonstrate that PiT-PO can generate symbolic equations tailored to turbulence modeling and that, under *a posteriori* CFD evaluation, the resulting predictions more closely match DNS references, which increases the practical value of LLM-based SR in real scientific and engineering workflows. With the proposed dual constraints,

PiT-PO provides targeted search and learning signals that enable the internalization of turbulence priors during equation discovery, thereby steering the model toward physically consistent and domain-relevant structures.

## 5 Related Work

Traditional SR has been studied through several lines, including genetic programming, reinforcement learning [31], and transformer-based generation [3]. Genetic programming [16] casts equation discovery as an evolutionary search over tree-structured programs, where candidate expressions are iteratively refined via mutation and crossover. Reinforcement learning-based SR, introduced by Petersen et al. [31], has developed into a family of policy-optimization frameworks [6, 8, 18, 29] that formulate SR as a sequential decision-making process. More recently, transformer-based models [14, 19, 45, 46, 53] have been adopted for SR, using large-scale pretraining to map numerical data directly to equations. However, these methods typically fail to incorporate scientific prior knowledge.

Recent progress in natural language processing has further enabled LLM-based SR methods, including LLM-SR [40], LaSR [10], ICSR [25], CoEvo [11], and SR-Scientist [51]. LLM-SR exploits scientific priors that are implicitly captured by LLMs to propose plausible functional forms, followed by data-driven parameter estimation. LaSR augments SR with abstract concept generation to guide

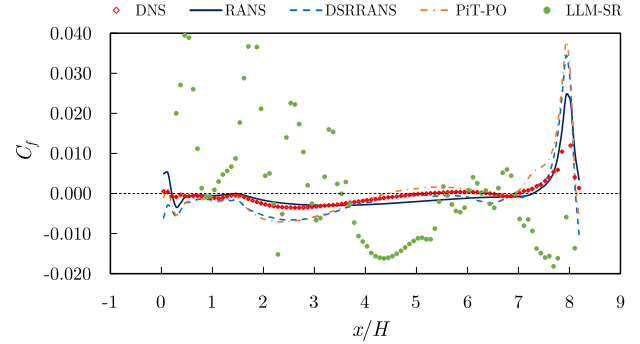


**Figure 7: Skin friction distribution along the bottom obtained by the learned model and the standard  $k-\omega$  SST model of RANS, compared with DNS data.**

hypothesis formation, while ICSR reformulates training examples as in-context prompts to elicit function generation. However, a unifying limitation across these methods is their reliance on the LLM as a frozen generator, which precludes incorporating search feedback to update the generation strategy and consequently restricts their ability to adapt to complex problems.

While some recent works, such as SOAR [33] and CALM [13], have begun to explore adaptive in-search tuning, they primarily focus on algorithm discovery or combinatorial optimization problems, whereas our method is specifically tailored for SR. By integrating hierarchical physical constraints and theorem-guided token regularization, PiT-PO establishes an adaptive framework capable of discovering accurate and physically consistent equations.

## 6 Conclusion

In this work, we introduced PiT-PO, a unified framework that fundamentally transforms LLMs from static equation proposers into adaptive, physics-aware generators for SR. By integrating in-search policy optimization with a novel dual-constraint evaluation mechanism, PiT-PO rigorously enforces hierarchical physical validity while leveraging theorem-guided, token-level penalties to eliminate structural redundancy. This synergistic design aligns generation with numerical fitness, scientific consistency, and parsimony, establishing new state-of-the-art performance on SR benchmarks. Beyond synthetic tasks, PiT-PO demonstrates significant practical utility in turbulence modeling, where the discovered symbolic corrections improve Reynolds stress and flow-field predictions. Notably, PiT-PO achieves these results using small open-source backbones, making it a practical and accessible tool for scientific communities with limited computational resources. Looking forward, we plan to extend PiT-PO to broader scientific and engineering domains by enriching the library of domain-specific constraints and validating it across more complex, real-world systems. Moreover, we anticipate that integrating PiT-PO with larger-scale multimodal foundation models could further unlock its potential in processing heterogeneous scientific data.

## References

[1] B. S. Aakash, JohnPatrick Connors, and Michael D Shields. 2019. Stress-strain data for aluminum 6061-T651 from 9 lots at 6 temperatures under uniaxial and plane strain tension. *Data in Brief* 25 (Aug 2019), 104085. doi:10.1016/j.dib.2019.104085

[2] Luca Biggio, Tommaso Bendinelli, Alexander Neitz, Aurelien Lucchi, and Giambattista Parascandolo. 2021. Neural Symbolic Regression that Scales. arXiv:2106.06427 [cs.LG] <https://arxiv.org/abs/2106.06427>

[3] L. Biggio\*, T. Bendinelli\*, A. Neitz, A. Lucchi, and G. Parascandolo. 2021. Neural Symbolic Regression that Scales. In *Proceedings of 38th International Conference on Machine Learning (ICML 2021) (Proceedings of Machine Learning Research, Vol. 139)*. PMLR, 936–945. <https://proceedings.mlr.press/v139/biggio21a.html> \*equal contribution.

[4] Jindou Chen, Jidong Tian, Liang Wu, ChenXinWei, Xiaokang Yang, Yaohui Jin, and Yanyan Xu. 2025. KinFormer: Generalizable Dynamical Symbolic Regression for Catalytic Organic Reaction Kinetics. In *International Conference on Representation Learning*, Y. Yue, A. Garg, N. Peng, F. Sha, and R. Yu (Eds.), Vol. 2025. 67058–67080. [https://proceedings.iclr.cc/paper\\_files/paper/2025/file/a76b693f36916a5ed84d6e5b39a0dc03-Paper-Conference.pdf](https://proceedings.iclr.cc/paper_files/paper/2025/file/a76b693f36916a5ed84d6e5b39a0dc03-Paper-Conference.pdf)

[5] Miles Cranmer. 2023. Interpretable Machine Learning for Science with PySR and SymbolicRegression.jl. arXiv:2305.01582 [astro-ph.IM] <https://arxiv.org/abs/2305.01582>

[6] Laure Crochepierre, Lydia Boudjeloud-Assala, and Vincent Barbesant. 2022. Interactive Reinforcement Learning for Symbolic Regression from Multi-Format Human-Preference Feedbacks. In *IJCAI 2022- 31st International Joint Conference on Artificial Intelligence*, Vienne, Austria. <https://hal.science/hal-03695471>

[7] Song Deng, Junjie Wang, Li Tao, Su Zhang, and Hongwei Sun. 2023. EV charging load forecasting model mining algorithm based on hybrid intelligence. *Computers and Electrical Engineering* 112 (2023), 109010. doi:10.1016/j.compeleceng.2023.109010

[8] Mengge Du, Yuntian Chen, and Dongxiao Zhang. 2023. DISCOVER: Deep identification of symbolically concise open-form PDEs via enhanced reinforcement-learning. arXiv:2210.02181 [cs.LG] <https://arxiv.org/abs/2210.02181>

[9] Roger Fletcher. 1987. *Practical Methods of Optimization* (2nd ed.). John Wiley & Sons, Chichester, New York.

[10] Arya Grayeli, Atharva Sehgal, Omar Costilla-Reyes, Miles Cranmer, and Swarat Chaudhuri. 2024. Symbolic Regression with a Learned Concept Library. arXiv:2409.09359 [cs.LG] <https://arxiv.org/abs/2409.09359>

[11] Ping Guo, Qingfu Zhang, and Xi Lin. 2025. CoEvo: Continual Evolution of Symbolic Solutions Using Large Language Models. arXiv:2412.18890 [cs.AI] <https://arxiv.org/abs/2412.18890>

[12] Edward J. Hu, Yelong Shen, Phillip Wallis, Zeyuan Allen-Zhu, Yuanzhi Li, Shean Wang, Lu Wang, and Weizhu Chen. 2021. LoRA: Low-Rank Adaptation of Large Language Models. arXiv:2106.09685 [cs.CL] <https://arxiv.org/abs/2106.09685>

[13] Ziyao Huang, Weiwei Wu, Kui Wu, Jianping Wang, and Wei-Bin Lee. 2025. CALM: Co-evolution of Algorithms and Language Model for Automatic Heuristic Design. arXiv:2505.12285 [cs.NE] <https://arxiv.org/abs/2505.12285>

[14] Pierre-Alexandre Kamienny, Stéphane d’Ascoli, Guillaume Lample, and François Charton. 2022. End-to-end symbolic regression with transformers. arXiv:2204.10532 [cs.LG] <https://arxiv.org/abs/2204.10532>

[15] Paul Kassianik, Baturay Saglam, Alexander Chen, Blaine Nelson, Anu Vellore, Massimo Aufiero, Fraser Burch, Dhruv Kedia, Avi Zohary, Sajana Weerawardhena, Aman Priyanshu, Adam Swanda, Amy Chang, Hyrum Anderson, Kojin Oshima, Omar Santos, Yaron Singer, and Amin Karbasi. 2025. Llama-3.1-FoundationAI-SecurityLLM-Base-8B Technical Report. arXiv:2504.21039 [cs.CR] <https://arxiv.org/abs/2504.21039>

[16] J.R. Koza. 1990. Genetically breeding populations of computer programs to solve problems in artificial intelligence. In *[1990] Proceedings of the 2nd International IEEE Conference on Tools for Artificial Intelligence*. 819–827. doi:10.1109/TAI.1990.130444

[17] Mikel Landajuela, Chak Shing Lee, Jiachen Yang, Ruben Glatt, Claudio P. Santiago, Ignacio Aravena, Terrell Mundhenk, Garrett Mulcahy, and Brenden K Petersen. 2022. A Unified Framework for Deep Symbolic Regression. In *Advances in Neural Information Processing Systems*, S. Koyejo, S. Mohamed, A. Agarwal, D. Belgrave, K. Cho, and A. Oh (Eds.), Vol. 35. Curran Associates, Inc., 33985–33998. [https://proceedings.neurips.cc/paper\\_files/paper/2022/file/dbea58f35bddd6e4003b2dd80e42f838-Paper-Conference.pdf](https://proceedings.neurips.cc/paper_files/paper/2022/file/dbea58f35bddd6e4003b2dd80e42f838-Paper-Conference.pdf)

[18] Mikel Landajuela, Brenden K. Petersen, Soo K. Kim, Claudio P. Santiago, Ruben Glatt, T. Nathan Mundhenk, Jacob F. Pettit, and Daniel M. Faissol. 2021. Improving exploration in policy gradient search: Application to symbolic optimization. arXiv:2107.09158 [cs.LG] <https://arxiv.org/abs/2107.09158>

[19] Wenqiang Li, Weijun Li, Linjun Sun, Min Wu, Lina Yu, Jingyi Liu, Yanjie Li, and Song Tian. 2023. Transformer-based model for symbolic regression via joint supervised learning. In *International Conference on Learning Representations*. <https://api.semanticscholar.org/CorpusID:259298765>

[20] Pingchuan Ma, Tsun-Hsuan Wang, Minghao Guo, Zhiqing Sun, Joshua B. Tenenbaum, Daniela Rus, Chuang Gan, and Wojciech Matusik. 2024. LLM and Simulation as Bilevel Optimizers: A New Paradigm to Advance Physical Scientific Discovery. In *Proceedings of the 41st International Conference on Machine Learning (Proceedings of Machine Learning Research, Vol. 235)*. Ruslan Salakhutdinov, Zico Kolter, Katherine Heller, Adrian Weller, Nuria Oliver, Jonathan Scarlett, and Felix Berkenkamp (Eds.). PMLR, 33940–33962. <https://proceedings.mlr.press/v235/ma24m.html>

[21] Nour Makke and Sanjay Chawla. 2024. Data-driven discovery of Tsallis-like distribution using symbolic regression in high-energy physics. *PNAS Nexus* 3, 11 (10 2024), pgea467. arXiv:<https://academic.oup.com/pnasnexus/article-pdf/3/11/pgea467/60816181/pgea467.pdf> doi:10.1093/pnasnexus/pgea467

[22] Nour Makke and Sanjay Chawla. 2024. Interpretable scientific discovery with symbolic regression: a review. *Artificial Intelligence Review* 57 (01 2024). doi:10.1007/s10462-023-10622-0

[23] Florian R Menter. 1994. Two-equation eddy-viscosity turbulence models for engineering applications. *AIAA journal* 32, 8 (1994), 1598–1605.

[24] Florian R Menter, Martin Kuntz, Robin Langtry, et al. 2003. Ten years of industrial experience with the SST turbulence model. *Turbulence, heat and mass transfer* 4, 1 (2003), 625–632.

[25] Matteo Merler, Katsiaryna Hartsuikovich, Nicola Dainese, and Pekka Marttinen. 2024. In-Context Symbolic Regression: Leveraging Large Language Models for Function Discovery. In *Proceedings of the 62nd Annual Meeting of the Association for Computational Linguistics (Volume 4: Student Research Workshop)*. Association for Computational Linguistics, 589–606. doi:10.18653/v1/2024.acl-srw.49

[26] Shinsuke MOCHIZUKI and Hideo OSAKA. 2000. Management of a Stronger Wall Jet by a Pair of Streamwise Vortices. Reynolds Stress Tensor and Production Tens. *TRANSACTIONS OF THE JAPAN SOCIETY OF MECHANICAL ENGINEERS Series B* 66, 646 (2000), 1309–1317. doi:10.1299/kikaib.66.646\_1309

[27] Peter A. Monkewitz. 2021. Asymptotics of streamwise Reynolds stress in wall turbulence. *Journal of Fluid Mechanics* 931 (Nov 2021). doi:10.1017/jfm.2021.924

[28] Jacques Monod. 1949. THE GROWTH OF BACTERIAL CULTURES. *Annual Review of Microbiology* 3, Volume 3, 1949 (1949), 371–394. doi:10.1146/annurev.mi.03.100149.002103

[29] T. Nathan Mundhenk, Mikel Landajuela, Ruben Glatt, Claudio P. Santiago, Daniel M. Faissol, and Brenden K. Petersen. 2021. Symbolic Regression via Neural-Guided Genetic Programming Population Seeding. arXiv:2111.00053 [cs.NE] <https://arxiv.org/abs/2111.00053>

[30] Iulian Neamtiu, Jeffrey S. Foster, and Michael Hicks. 2005. Understanding source code evolution using abstract syntax tree matching. In *Proceedings of the 2005 International Workshop on Mining Software Repositories* (St. Louis, Missouri) (MSR ’05). Association for Computing Machinery, New York, NY, USA, 1–5. doi:10.1145/1083142.1083143

[31] Brenden K. Petersen, Mikel Landajuela, T. Nathan Mundhenk, Claudio P. Santiago, Soo K. Kim, and Joanne T. Kim. 2021. Deep symbolic regression: Recovering mathematical expressions from data via risk-seeking policy gradients. arXiv:1912.04871 [cs.LG] <https://arxiv.org/abs/1912.04871>

[32] Stephen B. Pope. 2000. *Turbulent Flows*. Cambridge University Press. doi:10.1017/cbo9780511840531

[33] Julien POURCEL, Cédric COLAS, and Pierre-Yves Oudeyer. 2025. Self-Improving Language Models for Evolutionary Program Synthesis: A Case Study on ARCA-AGI. arXiv:2507.14172 [cs.LG] <https://arxiv.org/abs/2507.14172>

[34] Julia Reuter, Hani Elmestikawy, Fabien Evrard, Sanaz Mostaghim, and Berend van Wachem. 2023. Graph Networks as Inductive Bias for Genetic Programming: Symbolic Models for Particle-Laden Flows. In *Genetic Programming*, Gisele Pappa, Mario Giacobini, and Zdenek Vasicek (Eds.). Springer Nature Switzerland, Cham, 36–51.

[35] Bernardino ROMERA-PAREDES, Mohammadamin Barekatain, Alexander Novikov, Matej Balog, M Pawan Kumar, Emilien Dupont, Francisco JR Ruiz, Jordan S Ellenberg, Pengming Wang, Omar Fawzi, et al. 2024. Mathematical discoveries from program search with large language models. *Nature* 625, 7995 (2024), 468–475.

[36] L. Rosso, J. R. Lobry, S. Bajard, and J. P. Flandrois. 1995. Convenient Model To Describe the Combined Effects of Temperature and pH on Microbial Growth. *Applied and Environmental Microbiology* 61, 2 (Feb 1995), 610–6. doi:10.1128/aem.61.2.610-6.1995

[37] Michael Schmidt and Hod Lipson. 2009. Distilling Free-Form Natural Laws from Experimental Data. *Science* 324, 5923 (2009), 81–85. arXiv:<https://www.science.org/doi/pdf/10.1126/science.1165893> doi:10.1126/science.1165893

[38] Zhihong Shao, Peiyi Wang, Qihao Zhu, Runxin Xu, Junxiao Song, Xiao Bi, Haowei Zhang, Mingchuan Zhang, Y. K. Li, Y. Wu, and Daya Guo. 2024. DeepSeekMath: Pushing the Limits of Mathematical Reasoning in Open Language Models. arXiv:2402.03300 [cs.CL] <https://arxiv.org/abs/2402.03300>

[39] Hao Shi, Weili Song, Xinting Zhang, Jiahe Shi, Cuicui Luo, Xiang Ao, Hamid Arian, and Luis Seco. 2024. AlphaForge: A Framework to Mine and Dynamically Combine Formulaic Alpha Factors. arXiv:2406.18394 [q-fin.CP] <https://arxiv.org/abs/2406.18394>

[40] Parshin Shojaee, Kazem Meidani, Shashank Gupta, Amir Barati Farimani, and Chandan K Reddy. 2025. LLM-SR: Scientific Equation Discovery via Programming with Large Language Models. arXiv:2404.18400 [cs.LG] <https://arxiv.org/abs/2404.18400>

[41] Parshin Shojaee, Ngoc-Hieu Nguyen, Kazem Meidani, Amir Barati Farimani, Khoa D Doan, and Chandan K Reddy. 2025. LLM-SRBench: A New Benchmark for Scientific Equation Discovery with Large Language Models. arXiv:2504.10415 [cs.CL] <https://arxiv.org/abs/2504.10415>

[42] Hongwei Tang, Yan Wang, Tongguang Wang, and Linlin Tian. 2023. Discovering explicit Reynolds-averaged turbulence closures for turbulent separated flows through deep learning-based symbolic regression with non-linear corrections. *Physics of Fluids* 35, 2 (2023), 025118. arXiv:<https://doi.org/10.1063/5.0135638> doi:10.1063/5.0135638

[43] Hongwei Tang, Yan Wang, Tongguang Wang, and Linlin Tian. 2023. Discovering explicit Reynolds-averaged turbulence closures for turbulent separated flows through deep learning-based symbolic regression with non-linear corrections. *Physics of Fluids* 35, 2 (Feb. 2023). doi:10.1063/5.0135638

[44] Henk Tennekes and John L. Lumley. 1972. *A First Course in Turbulence*. The MIT Press. doi:10.7551/mitpress/3014.001.0001

[45] Mojtaba Valipour, Bowen You, Maysum Panju, and Ali Ghodsi. 2021. SymbolicGPT: A Generative Transformer Model for Symbolic Regression. arXiv:2106.14131 [cs.LG] <https://arxiv.org/abs/2106.14131>

[46] Martin Vastl, Jonaš Kulhánek, Jiří Kubalík, Erik Derner, and Robert Babuška. 2024. SymFormer: End-to-End Symbolic Regression Using Transformer-Based Architecture. *IEEE Access* 12 (2024), 37840–37849. doi:10.1109/ACCESS.2024.3374649

[47] Marco Virgolin and Solon P. Pissis. 2022. Symbolic Regression is NP-hard. arXiv:2207.01018 [cs.NE] <https://arxiv.org/abs/2207.01018>

[48] Ylva Wahlquist, Jesper Sundell, and Kristian Soltész. 2024. Learning pharmacometric covariate model structures with symbolic regression networks. *Journal of Pharmacokinetics and Pharmacodynamics* 51, 2 (2024), 155–167. doi:10.1007/s10928-023-09887-3

[49] Wei WANG, Yang ZHANG, and Lili CHEN. 2019. An application of the shear stress transport low-Reynolds-number k-ε turbulence model on turbulent flows. *ACTA AERODYNAMICA SINICA* 37, 3 (2019), 419–425. doi:10.7638/kqdlxxb-2016.0158

[50] H.G. Weller, Gavin Tabor, Hrvoje Jasak, and Christer Fureby. 1998. A Tensorial Approach to Computational Continuum Mechanics Using Object Orientated Techniques. *Computers in Physics* 12 (11 1998), 620–631. doi:10.1063/1.1168744

[51] Shijie Xia, Yuhua Sun, and Pengfei Liu. 2025. SR-Scientist: Scientific Equation Discovery With Agentic AI. arXiv:2510.11661 [cs.AI] <https://arxiv.org/abs/2510.11661>

[52] Heng Xiao, Jin-Long Wu, Sylvain Laizet, and Lian Duan. 2020. Flows over periodic hills of parameterized geometries: A dataset for data-driven turbulence modeling from direct simulations. *Computers & Fluids* 200 (2020), 104431. doi:10.1016/j.compfluid.2020.104431

[53] Hengzhe Zhang, Qi Chen, Bing XUE, Wolfgang Banzhaf, and Mengjie Zhang. 2025. RAG-SR: Retrieval-Augmented Generation for Neural Symbolic Regression. In *The Thirteenth International Conference on Learning Representations*. <https://openreview.net/forum?id=NdHka08uWn>

## A Additional Hyperparameters of PiT-PO

Table 3 lists the additional hyperparameters of PiT-PO, including (i) general-level physical penalties (dimensional homogeneity and differentiability), (ii) domain-specific constraint penalties, (iii) the gated activation threshold for physical constraints, and (iv) theorem-guided redundancy detection and token-level penalization.

## B Support Exclusion Theorem: Theory and Practice

### B.1 Preliminaries: Empirical Function Space and Orthogonality

*Definition B.1 (Basis functions / dictionary).* Let  $\mathcal{X} \subseteq \mathbb{R}^d$  be the domain, and let  $\{\phi_j : \mathcal{X} \rightarrow \mathbb{R}\}_{j \in \mathcal{S}}$  be a collection of candidate basis (dictionary) functions indexed by  $\mathcal{S}$ . For any subset  $\mathcal{K} \subseteq \mathcal{S}$ , denote the corresponding model subspace by

$$\text{span}\{\phi_j : j \in \mathcal{K}\}.$$

*Definition B.2 (Target function  $f^*$ ).* Assume the ground-truth target function admits a sparse expansion over the dictionary:

$$f^*(x) = \sum_{j \in \mathcal{S}'} a_j \phi_j(x),$$

where  $\mathcal{S}' \subseteq \mathcal{S}$  is the true support set (indices of nonzero terms) and satisfies  $|\mathcal{S}'| \leq M$ . Moreover, the true coefficients are bounded as

$$A \leq |a_j| \leq B, \quad \forall j \in \mathcal{S}'.$$

*Definition B.3 (Empirical inner product and empirical norm).* Given a finite dataset  $D = \{x_n\}_{n=1}^N \subset \mathcal{X}$ , for any two functions  $f, g : \mathcal{X} \rightarrow \mathbb{R}$ , define the empirical inner product by

$$\langle f, g \rangle_D := \frac{1}{N} \sum_{n=1}^N f(x_n) g(x_n),$$

and the induced empirical norm by

$$\|f\|_D := \sqrt{\langle f, f \rangle_D}.$$

The empirical function space

$$\mathcal{F}_D := \{(f(x_1), \dots, f(x_N)) : f : \mathcal{X} \rightarrow \mathbb{R}\}$$

is a finite-dimensional inner-product space under  $\langle \cdot, \cdot \rangle_D$ .

*Definition B.4 (Empirical Orthogonality).* Two functions  $f, g \in \mathcal{F}_D$  are empirically orthogonal if  $\langle f, g \rangle_D = 0$ .

**Convention.** Unless stated otherwise, throughout this appendix we write  $\langle \cdot, \cdot \rangle$  and  $\| \cdot \|$  to mean the empirical inner product  $\langle \cdot, \cdot \rangle_D$  and the empirical norm  $\| \cdot \|_D$ .

### B.2 Proof of the Support Exclusion Theorem

**THEOREM B.5 (SUPPORT EXCLUSION THEOREM).** Let  $\mathcal{K} \subseteq \mathcal{S}$  be a candidate skeleton (active set). Consider the empirical least-squares fit over  $\mathcal{K}$ :

$$b \in \arg \min_{\{b_j\}_{j \in \mathcal{K}}} \left\| f^* - \sum_{j \in \mathcal{K}} b_j \phi_j \right\|^2.$$

Define the empirical Gram matrix  $G \in \mathbb{R}^{|\mathcal{S}| \times |\mathcal{S}|}$  by

$$G_{ij} := \langle \phi_i, \phi_j \rangle, \quad i, j \in \mathcal{S},$$

Component	Symbol	Value	Notes
Fitting log-MSE scale	$\alpha$	1.0	Scaling in $R_{\text{fit}} = -\alpha \log(\text{MSE} + \epsilon)$ .
Complexity penalty weight	$\lambda_{\text{len}}$	5e-3	Weight in $P_{\text{cplx}} = \lambda_{\text{len}} \cdot \text{Length}(\text{AST})$ .
Dimensional homogeneity penalty weight	$P_{\text{dim}}$	1.0	Penalty/reward weight for unit inconsistency (general-level constraint).
Differentiability penalty weight	$P_{\text{diff}}$	0.5	Penalty/reward weight for non-smoothness on the data-defined domain (general-level constraint).
Domain-specific constraint weight (j-th)	$P_{\text{domain}}^{(j)}$	0.5	Weight for the $j$ -th domain prior (e.g., realizability, wall BC, asymptotic scaling, energy consistency).
Gating threshold for physics constraints	$\delta_{\text{gate}}$	1e-3 * MSE_{initial}	Activate physics penalties only after fitting reaches a sufficiently low-error regime.
Numerical stability constant in $\tau_i$	$\epsilon$	1e-50	Used in $\tau_i = \frac{ b_i }{\sum_j  b_j  + \epsilon}$ to avoid division by zero.
Redundancy threshold	$\rho$	1e-2	A term is considered redundant if $\tau_i \leq \rho$ .
Token penalty scale	$p$	0.5	Scaling coefficient in $P_{\text{tok}} = p \cdot \max(0, -\log( b_i  + \epsilon))$ .

Table 3: Hyperparameters for dual-constraint evaluation and token-level signal synthesis.

and assume  $G_{ii} > 0$ . For any  $i \in \mathcal{S}$ , define

$$T_{ij} := \frac{G_{ji}}{G_{ii}}, \quad j \in \mathcal{S}.$$

Further define the external-candidate vector

$$u_i := (|T_{il}|)_{l \in \mathcal{S} \setminus \mathcal{K}} \in \mathbb{R}^{|\mathcal{S} \setminus \mathcal{K}|},$$

and let  $s(1) \geq s(2) \geq \dots \geq s(|\mathcal{S} \setminus \mathcal{K}|)$  be the entries of  $u_i$  sorted in non-increasing order. If for some  $i \in \mathcal{K}$ ,

$$|b_i| < A - \left( \underbrace{\sum_{j \in \mathcal{K}, j \neq i} (B + |b_j|) |T_{ij}|}_{\text{Internal Interference}} + \underbrace{B \sum_{k=1}^{|\mathcal{S} \setminus \mathcal{K}|} s(k)}_{\text{External Interference}} \right),$$

then  $i \notin \mathcal{S}'$ .

**PROOF.** **Step 1: Empirical orthogonality (first-order optimality of least squares).** Let

$$g(x) := \sum_{j \in \mathcal{K}} b_j \phi_j(x), \quad r(x) := f^*(x) - g(x).$$

The objective is  $\|r\|^2 = \langle r, r \rangle$ . For any  $i \in \mathcal{K}$ , the first-order optimality condition yields

$$0 = \frac{\partial}{\partial b_i} \|r\|^2 = -2 \langle r, \phi_i \rangle \implies \langle r, \phi_i \rangle = 0.$$

Hence, the residual  $r$  is empirically orthogonal to  $\text{span}\{\phi_i : i \in \mathcal{K}\}$ .

**Step 2: Set decomposition.** Define three disjoint sets

$$\mathcal{T} := \mathcal{K} \cap \mathcal{S}', \quad \mathcal{F} := \mathcal{K} \setminus \mathcal{S}', \quad \mathcal{R} := \mathcal{S}' \setminus \mathcal{K}.$$

Then  $\mathcal{K} = \mathcal{T} \cup \mathcal{F}$  and  $\mathcal{S}' = \mathcal{T} \cup \mathcal{R}$ . Expanding the residual gives

$$r = \sum_{j \in \mathcal{T}} (a_j - b_j) \phi_j + \sum_{j \in \mathcal{R}} a_j \phi_j - \sum_{j \in \mathcal{F}} b_j \phi_j.$$

**Step 3: An exact coefficient identity for  $i \in \mathcal{T}$ .** Fix any  $i \in \mathcal{T} \subseteq \mathcal{K}$ . Using  $\langle r, \phi_i \rangle = 0$  and writing  $G_{ji} = \langle \phi_j, \phi_i \rangle$ , we obtain

$$(a_i - b_i) G_{ii} + \sum_{j \in \mathcal{T}, j \neq i} (a_j - b_j) G_{ji} + \sum_{j \in \mathcal{R}} a_j G_{ji} - \sum_{j \in \mathcal{F}} b_j G_{ji} = 0.$$

Dividing by  $G_{ii} > 0$  and using  $T_{ij} = G_{ji}/G_{ii}$  yields

$$a_i - b_i = - \sum_{j \in \mathcal{T}, j \neq i} (a_j - b_j) T_{ij} - \sum_{j \in \mathcal{R}} a_j T_{ij} + \sum_{j \in \mathcal{F}} b_j T_{ij}.$$

**Step 4: Upper bound via internal and external interference.** Taking absolute values and applying the triangle inequality gives

$$|a_i - b_i| \leq \sum_{j \in \mathcal{T}, j \neq i} |a_j - b_j| |T_{ij}| + \sum_{j \in \mathcal{R}} |a_j| |T_{ij}| + \sum_{j \in \mathcal{F}} |b_j| |T_{ij}|.$$

For  $j \in \mathcal{T} \subseteq \mathcal{S}'$ , we have  $|a_j| \leq B$  and thus

$$|a_j - b_j| \leq |a_j| + |b_j| \leq B + |b_j|.$$

Therefore,

$$|a_i - b_i| \leq \sum_{j \in \mathcal{T}, j \neq i} (B + |b_j|) |T_{ij}| + \sum_{j \in \mathcal{F}} |b_j| |T_{ij}| + B \sum_{j \in \mathcal{R}} |T_{ij}|.$$

Since  $|b_j| \leq B + |b_j|$  for all  $j \in \mathcal{F}$ , we further have

$$\sum_{j \in \mathcal{F}} |b_j| |T_{ij}| \leq \sum_{j \in \mathcal{F}} (B + |b_j|) |T_{ij}|.$$

Combining  $\mathcal{T} \setminus \{i\}$  and  $\mathcal{F}$  yields the internal-interference term:

$$|a_i - b_i| \leq \underbrace{\sum_{j \in \mathcal{K}, j \neq i} (B + |b_j|) |T_{ij}|}_{\text{Internal Interference}} + B \sum_{j \in \mathcal{R}} |T_{ij}|.$$

For the external term, note that  $\mathcal{R} \subseteq \mathcal{S} \setminus \mathcal{K}$ , and the entries  $\{|T_{il}|_{l \in \mathcal{S} \setminus \mathcal{K}}\}$  sorted in non-increasing order are  $s(1) \geq \dots \geq s(|\mathcal{S} \setminus \mathcal{K}|)$ . Hence, for any subset  $\mathcal{R}$ ,

$$\sum_{j \in \mathcal{R}} |T_{ij}| \leq \sum_{k=1}^{|\mathcal{R}|} s(k).$$

Assuming  $|\mathcal{S}'| \leq M$  and that the current support is partially correct, i.e.,  $\mathcal{K} \cap \mathcal{S}' \neq \emptyset$ , we have  $|\mathcal{R}| = |\mathcal{S}' \setminus \mathcal{K}| \leq |\mathcal{S}'| - 1 \leq M - 1$ . Define  $m := \min(M - 1, |\mathcal{S} \setminus \mathcal{K}|)$ . Since also  $|\mathcal{R}| \leq |\mathcal{S} \setminus \mathcal{K}|$ , it follows that  $|\mathcal{R}| \leq m$ , and thus

$$\sum_{j \in \mathcal{R}} |T_{ij}| \leq \sum_{k=1}^{|\mathcal{R}|} s(k) \leq \sum_{k=1}^m s(k).$$

Thus,

$$|a_i - b_i| \leq \sum_{j \in \mathcal{K}, j \neq i} (B + |b_j|) |T_{ij}| + B \sum_{k=1}^m s(k).$$

**Step 5: Lower bound when  $i \in \mathcal{S}'$ .** If  $i \in \mathcal{S}'$ , then  $|a_i| \geq A$ . By the reverse triangle inequality,

$$|a_i - b_i| \geq ||a_i| - |b_i|| \geq A - |b_i|.$$

**Step 6: Contradiction.** Assume, for contradiction, that there exists  $i \in \mathcal{K} \cap \mathcal{S}'$  satisfying

$$|b_i| < A - \left( \sum_{j \in \mathcal{K}, j \neq i} (B + |b_j|) |T_{ij}| + B \sum_{k=1}^m s(k) \right).$$

Rearranging yields

$$A - |b_i| > \sum_{j \in \mathcal{K}, j \neq i} (B + |b_j|) |T_{ij}| + B \sum_{k=1}^m s(k).$$

However, Step 5 implies  $|a_i - b_i| \geq A - |b_i|$ , while the bound above implies

$$|a_i - b_i| \leq \sum_{j \in \mathcal{K}, j \neq i} (B + |b_j|) |T_{ij}| + B \sum_{k=1}^m s(k),$$

which is a contradiction. Therefore such an  $i$  cannot belong to  $\mathcal{S}'$ , i.e.,  $i \notin \mathcal{S}'$ .  $\square$

## C Supplementary Diagnostics and Analyses

### C.1 Remaining Iteration Curves on Smaller Backbones

In the main text, we report iteration curves for the 8B backbone. Here we provide the remaining curves for 3B and 1B (Figure 8), which corroborate the observations in Section 4.4.

### C.2 Time-Cost Analysis under a Fixed Wall-Clock Budget

To complement the iteration-based efficiency analysis in Section 4.4, we evaluate search efficiency under a strict wall-clock constraint. We fix the total runtime of each method to 25,000 seconds ( $\approx 6.9$  hours) and track the best-so-far NMSE as a function of elapsed time (Figure 9). This protocol directly answers a practical question: given the same compute time, which method returns a more accurate recovered equation?

Across all three backbones (Llama-3.1-8B, Llama-3.2-3B, and Llama-3.2-1B), PiT-PO consistently yields lower NMSE trajectories than LLM-SR under the same 25,000-second budget. In line with the behavior discussed in Section 4.4, the curves exhibit a characteristic divergence in the low-error regime: LLM-SR often plateaus after an initial reduction, while PiT-PO continues to realize step-wise decreases over time, indicating more effective late-stage credit assignment and continued progress rather than stagnation.

The advantage is most pronounced on the two oscillator systems. For 8B and 3B, PiT-PO achieves rapid early improvements and maintains additional phase transitions later in the run, reaching substantially lower NMSE within the same wall-clock budget. For the 1B model, both methods converge more slowly overall, yet PiT-PO still more reliably escapes stagnation and attains markedly

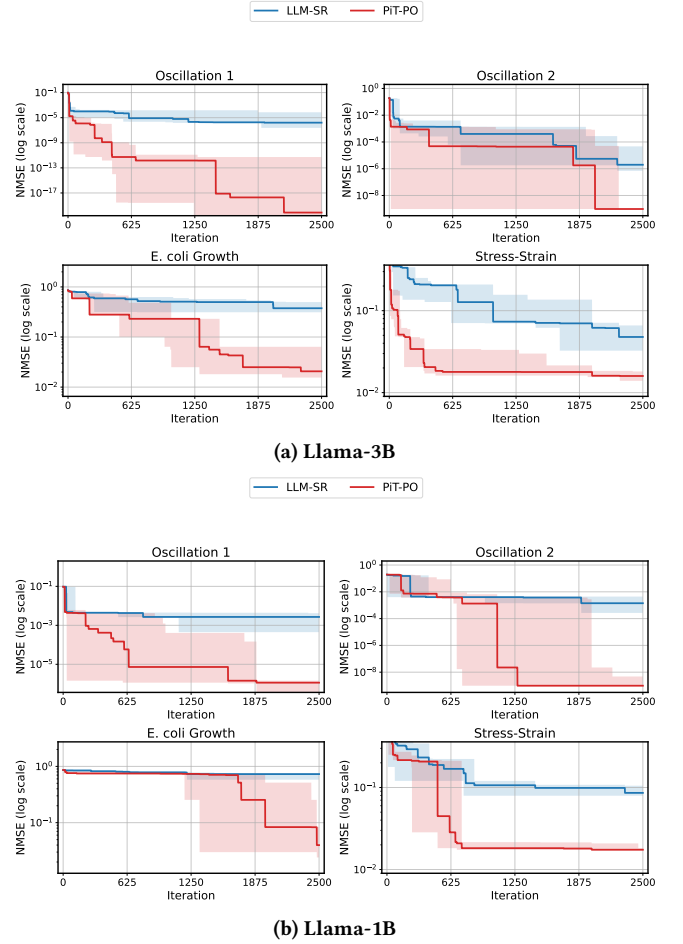


**Figure 8: NMSE versus iteration on smaller backbones, consistent with the trends in the 8B setting.**

lower final NMSE, suggesting that the proposed in-search tuning remains effective even in the small-model regime.

Similar trends hold for the E. coli Growth and Stress-Strain tasks, where progress is typically more gradual. Under equal wall-clock time, PiT-PO achieves a lower final NMSE and exhibits clearer late-stage improvements, whereas LLM-SR tends to flatten earlier. Importantly, these gains are obtained without increasing runtime: despite the additional overhead introduced by in-search policy optimization, PiT-PO delivers consistently better return-on-compute within a fixed time budget, validating the practical efficiency of the proposed approach.

### C.3 OOD Evaluation (NMSE<sub>OOD</sub>)

We report out-of-distribution performance using NMSE on the OOD split (NMSE<sub>OOD</sub>), summarized in Table 4. Across all three backbones (8B/3B/1B) and all four tasks, PiT-PO achieves lower NMSE<sub>OOD</sub> than LLM-SR under the same setting. In particular, PiT-PO maintains extremely small OOD errors on the two oscillator systems, and yields substantially reduced OOD NMSE on E. coli growth and Stress-Strain, where LLM-SR exhibits noticeably larger errors.

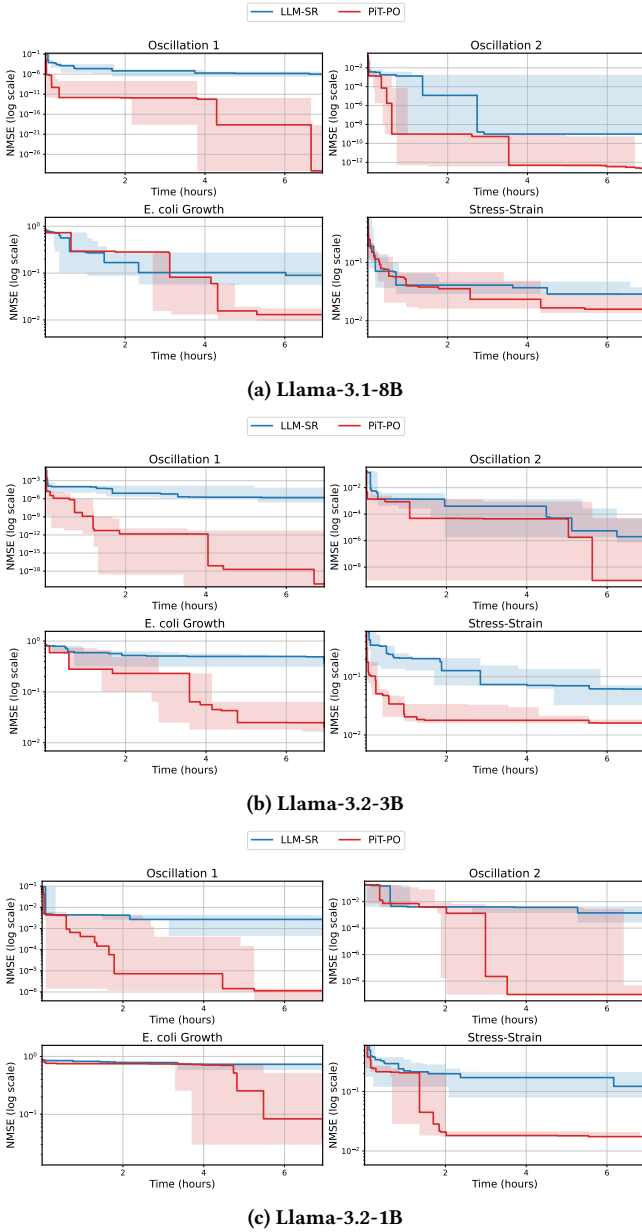


Figure 9: Wall-clock efficiency under a fixed 25,000-second budget.

These results provide consistent evidence that the improvements observed in the main text persist under OOD evaluation.

#### C.4 Equation Iterative Trajectories

Figure 10 visualizes how symbolic structures evolve along the iterative search. For PiT-PO (Figure 10a), the trajectory reveals a clear process of progressively excluding spurious terms. Under the theorem-guided mathematical constraints and the token-aware policy update, tokens marked as redundant are assigned token-level penalties; as this penalty signal repeatedly accumulates across many

Method	Oscillator1	Oscillator2	E. coli growth	Stress-Strain
	NMSE <sub>OOD</sub> ↓	NMSE <sub>OOD</sub> ↓	NMSE <sub>OOD</sub> ↓	NMSE <sub>OOD</sub> ↓
LLM-SR (Llama-3.1-8B)	0.0114	8.05e-10	0.1676	0.1026
LLM-SR (Llama-3.2-3B)	0.0191	5.56e-5	809.94	0.0264
LLM-SR (Llama-3.2-1B)	0.1182	7.57e-3	1888.5	0.2689
PiT-PO (Llama-3.1-8B)	<b>1.63e-30</b>	<b>1.36e-11</b>	0.1163	0.0163
PiT-PO (Llama-3.2-3B)	<b>2.63e-30</b>	8.52e-10	<b>0.0237</b>	0.0144
PiT-PO (Llama-3.2-1B)	5.99e-5	8.58e-10	0.3462	<b>0.0124</b>

Table 4: OOD evaluation: NMSE on the OOD split.

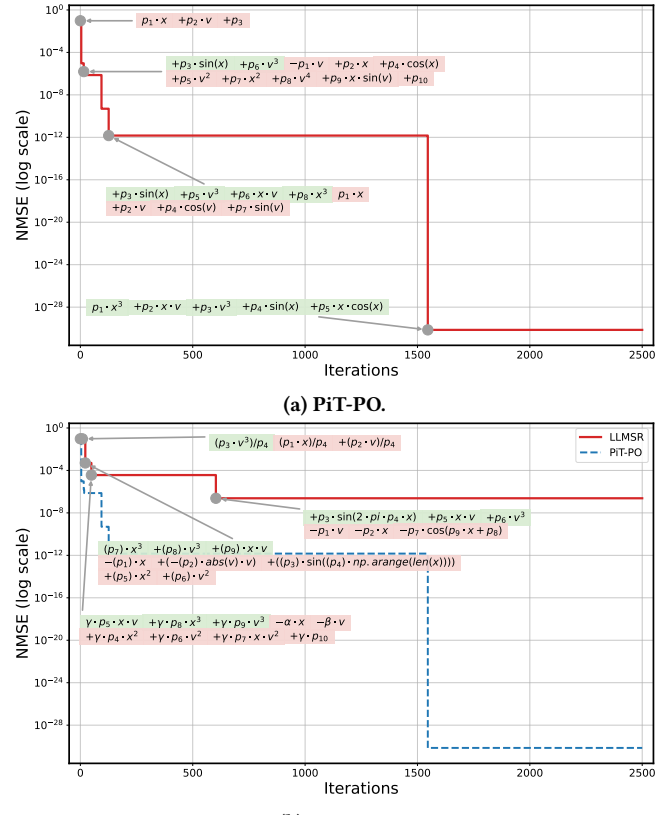


Figure 10: Iterative trajectories of PiT-PO and LLM-SR on Oscillator1 with Llama-3.1-8B-Instruct. The NMSE curves (log scale) report the best-so-far value over iterations. Annotated equation snapshots illustrate how the discovered structure evolves along the search trajectory. The green-shaded terms are correct, whereas the red-shaded terms are erroneous.

sampled equations during optimization, such spurious components become progressively less preferred and are unlikely to reappear in later generations. As a result, the search does not merely fit numerically; instead, it repeatedly transitions to cleaner structures, and each step-wise NMSE drop aligns with the removal of nuisance terms and a move toward a more parsimonious functional form. This “error-term elimination” behavior effectively shrinks the search space and substantially strengthens the exploration capability.

In contrast, LLM-SR (Figure 10b) exhibits much weaker structural correction. Since its guidance is primarily prompt-level rather than parameter-level, terms that appear early—even if structurally incorrect—tend to persist and continue influencing subsequent proposals. Consequently, the search frequently enters a plateau where NMSE stops improving meaningfully: the method keeps revisiting or retaining earlier spurious components instead of systematically pruning them, indicating a stagnation regime with limited ability to reach the correct structure.

## D Datasets

### D.1 LLM-SR Suite

We use the LLM-SR SUITE, which consists of four standard scientific equation discovery tasks spanning physics, biology, and materials science. The suite includes two nonlinear oscillator systems (Oscillation 1/2), an *E. coli* growth model (*E. coli* Growth), and a temperature-dependent stress-strain dataset (Stress–Strain). The first three tasks are dynamical systems and are simulated over a fixed time horizon, while the last task is a static constitutive relation evaluated on experimental measurements.

**D.1.1 Oscillation 1 (Nonlinear Oscillator).** Nonlinear oscillators with dissipative and non-polynomial couplings provide a demanding test for recovering interacting terms from trajectories. We define the state as  $x(t)$  and  $v(t) = \dot{x}(t)$ , and simulate the following system:

$$\begin{aligned}\dot{x} &= v, \\ \dot{v} &= F \sin(\omega x) - \alpha v^3 - \beta x^3 - \gamma xv - x \cos(x).\end{aligned}$$

We set  $F = 0.8$ ,  $\alpha = 0.5$ ,  $\beta = 0.2$ ,  $\gamma = 0.5$ , and  $\omega = 1.0$ , with initial conditions  $x(0) = 0.5$ ,  $v(0) = 0.5$ , and simulate over  $t \in [0, 50]$ .

**D.1.2 Oscillation 2 (Nonlinear Oscillator).** The second oscillator introduces explicit time forcing and an exponential nonlinearity, leading to a different coupling pattern between  $x$  and  $v$ :

$$\begin{aligned}\dot{x} &= v, \\ \dot{v} &= F \sin(\omega t) - \alpha v^3 - \beta xv - \delta x \exp(\gamma x).\end{aligned}$$

We use  $F = 0.3$ ,  $\alpha = 0.5$ ,  $\beta = 1.0$ ,  $\delta = 5.0$ ,  $\gamma = 0.5$ , and  $\omega = 1.0$ . The initial conditions and simulation window are the same as Oscillation 1:  $x(0) = 0.5$ ,  $v(0) = 0.5$ ,  $t \in [0, 50]$ .

**D.1.3 *E. coli* Growth (Bacterial Growth).** This task models the growth rate of *E. coli* as a product of multiplicative factors capturing distinct physiological effects from population size, nutrient availability, temperature, and acidity:

$$\frac{dB}{dt} = f_B(B) \cdot f_S(S) \cdot f_T(T) \cdot f_{\text{pH}}(\text{pH}),$$

where  $B$  is bacterial density,  $S$  is nutrient concentration,  $T$  is temperature, and  $\text{pH}$  denotes acidity. In our benchmark, the explicit functional form is:

$$\frac{dB}{dt} = \mu_{\max} B \left( \frac{S}{K_S + S} \right) \left( \frac{\tanh k(T - x_0)}{1 + c(T - x_{\text{decay}})^4} \right) \exp(-|\text{pH} - \text{pH}_{\text{opt}}|) \sin \left( \frac{(\text{pH} - \text{pH}_{\min})\pi}{\text{pH}_{\max} - \text{pH}_{\min}} \right)^2.$$

This specification combines saturation kinetics, sharp temperature modulation, and a structured pH response, yielding a challenging multivariate nonlinear discovery setting.

**D.1.4 Stress–Strain (Material Stress Behavior).** To assess performance on experimental measurements, we consider tensile stress–strain data for Aluminum 6061-T651 collected at multiple temperatures (from room temperature up to 300°C). While no single exact governing equation is provided, a commonly used phenomenological approximation for temperature-dependent hardening is:

$$\sigma = (A + B\varepsilon^n) \left( 1 - \left( \frac{T - T_r}{T_m - T_r} \right)^m \right).$$

where  $\sigma$  is stress,  $\varepsilon$  is strain,  $T$  is temperature,  $T_r$  is a reference temperature, and  $T_m$  is the melting temperature. The coefficients  $A$ ,  $B$ ,  $n$ , and  $m$  are fitted from data for the given alloy.

### D.2 LLM-SRBench

We additionally report results on LLM-SRBENCH, a benchmark specifically constructed to evaluate *data-driven* scientific equation discovery with LLMs while reducing the risk of trivial memorization of canonical textbook formulas. It contains 239 problems spanning four scientific domains (chemistry, biology, physics, and material science), and each task is packaged with (i) a short scientific context describing variables and the target quantity and (ii) tabular numerical samples used for discovery.

*Dataset composition.* LLM-SRBENCH is organized into two complementary subsets.

**(1) LSR-Transform.** This subset converts well-known physics equations into less-common but analytically equivalent forms by changing the prediction target. Concretely, starting from the original equation, one input variable is chosen as a *pivot* and promoted to the new target; the equation is then symbolically solved (e.g., via SymPy) for that pivot variable, yielding an alternative representation of the same underlying physical law. Only transformations that admit an analytic solution are retained, and the original datapoints are filtered to satisfy the valid domain of the transformed expression (e.g., avoiding invalid denominators or square-root domains). Finally, a new natural-language problem statement is generated to match the transformed input–output specification. This pipeline produces 111 transformed problems.

**(2) LSR-Synth.** This subset is designed to test discovery beyond memorized templates by composing equations from both *known* scientific terms and *synthetic* (novel yet plausible) terms. Candidate known/synthetic terms are proposed with an LLM given the domain context, combined into full equations, and then filtered through multiple checks: numerical solvability (e.g., via standard ODE solvers for dynamical systems), novelty assessment in context (using an LLM-based novelty evaluator), and expert plausibility validation. After passing these filters, datapoints are generated for each approved equation, yielding 128 synthetic problems across the same four domains.

*Symbolic Accuracy (SA).* Besides numeric fit metrics (e.g., NMSE and  $\text{Acc}_{\text{all}}(\tau)$ ), LLM-SRBENCH emphasizes *symbolic correctness*. Symbolic Accuracy (SA) is computed using an LLM-based equivalence judge (GPT-4o): given a predicted hypothesis and the ground-truth expression, the evaluator first normalizes both by removing extraneous text (e.g., comments) and replacing explicit numeric constants with placeholder parameters, then decides whether there exist parameter values that make the hypothesis mathematically

equivalent to the ground truth. SA is the fraction (percentage) of problems judged equivalent under this protocol. The benchmark authors validated this evaluation by comparing against human judgments on 130 sampled problems and reported 94.6% agreement between GPT-4o and human evaluators.

## E Turbulence Task Setup: Periodic Hill Flow

### E.1 Dataset

We consider the periodic hill flow configuration with streamwise periodic boundary conditions and no-slip walls.

In this work, the features selected for the symbolic regression process are computed from the mean strain-rate ( $S$ ) and rotation-rate ( $R$ ) tensors. Following established practice, these tensors are normalized using local turbulence scales prior to invariant calculation to ensure well-conditioned inputs:

$$S = \frac{1}{2} \frac{1}{\beta^* \omega} [\nabla u + (\nabla u)^\top], \quad (13)$$

$$R = \frac{1}{2} \frac{1}{\beta^* \omega} [\nabla u - (\nabla u)^\top], \quad (14)$$

where  $(\cdot)^\top$  denotes matrix transposition. The invariants are then computed as  $I_1 = \text{Tr}(S^2)$  and  $I_2 = \text{Tr}(R^2)$ .

The dataset provides (i) two invariant features  $(I_1, I_2)$  (stored in the `Lambda` columns), (ii) tensor bases  $\{T^m\}_{m=1}^3$  (stored in the first three  $3 \times 3$  tensors in the `Tensor` columns), and (iii) the target anisotropy tensor field  $b$  (and its nonlinear correction form used for training, denoted by  $b^\perp$ ), together with auxiliary fields such as turbulent kinetic energy  $k$  when needed by the evaluator.

#### E.1.1 Data Collection.

*DNS source.* The DNS data are obtained from the publicly available NASA turbulence modeling resource (*Turbulence Modeling Resource / TMBWG*) for periodic hills of parameterized geometries.<sup>1</sup>

*RANS baseline generation (for non-DNS methods).* For all non-DNS methods, we compute baseline solutions using OpenFOAM with the same initial and boundary conditions as the DNS. Specifically, we employ the incompressible steady-state solver `simpleFoam` and apply the turbulence models considered in this paper (all belonging to RANS and its SST variants). The solver outputs, at each sampling point and converged iteration/time-step, the required physical quantities for subsequent post-processing.

*DNS-RANS grid alignment and target construction.* To construct training targets consistent with the RANS discretization, we interpolate the DNS fields onto the RANS grid points. The interpolated DNS quantities are then post-processed *in the CFD workflow* (i.e., as offline preprocessing prior to training) to compute the Reynolds stress tensor, which is packaged into the dataset files as the supervision signal for training.

*Feature & basis construction.* Following Pope's tensor-basis expansion hypothesis, the Reynolds stress decomposition involves (i) tensor bases and (ii) scalar coefficient functions of invariant features. Since our final turbulence closure is embedded as a correction to the baseline kOmegaSST model, we use the physical fields

<sup>1</sup>[https://tmbwg.github.io/turbmodels/Other\\_DNS\\_Data/parameterized\\_periodic\\_hills.html](https://tmbwg.github.io/turbmodels/Other_DNS_Data/parameterized_periodic_hills.html)

produced by the baseline kOmegaSST computation for post-processing to obtain the input features and the tensor bases. These are stored in separate files (features and bases), while the learning target is defined to match the Reynolds-stress-related quantity described in Section E.2.

*E.1.2 Pre-processing.* We normalize the two invariant inputs prior to feeding them into the learned symbolic expressions:

$$\tilde{I} = \tanh\left(\frac{I}{2.0}\right), \quad \tilde{I}_1 = \tanh\left(\frac{I_1}{2.0}\right), \quad \tilde{I}_2 = \tanh\left(\frac{I_2}{2.0}\right), \quad (15)$$

which maps the raw values into approximately  $[-1, 1]$  and improves numerical stability during parameter fitting.

### E.2 Casting Turbulence Closure as a Symbolic Regression Problem

*Predicting scalar coefficients instead of tensor entries.* Rather than directly searching over tensor-valued symbolic forms, we let the LLM predict three scalar coefficient functions  $(G^1, G^2, G^3)$ , each parameterized as a symbolic expression of only two variables  $(I_1, I_2)$ . The evaluator then reconstructs the predicted tensor via the (fixed) tensor bases:

$$\hat{b} = G^1(I_1, I_2)T^1 + G^2(I_1, I_2)T^2 + G^3(I_1, I_2)T^3. \quad (16)$$

This design compresses the LLM input variable dimension to two, significantly reducing the symbolic search space.

*Scoring by MSE in the evaluator.* Given a candidate hypothesis, we compute the fitting score by the mean squared error between the target tensor and the reconstructed tensor. In the final evaluator, we additionally scale both prediction and target by the sample-wise  $k$  before error aggregation:

$$\hat{\tau}_{ij}(x_n) = k(x_n) \hat{b}_{ij}(x_n), \quad \tau_{ij}(x_n) = k(x_n) b_{ij}(x_n), \quad (17)$$

We compute the MSE only over a selected subset of tensor components. This is because the Reynolds-stress (and anisotropy) tensor is symmetric, so only six components are independent, and in the present periodic hill flow setting two off-plane shear components are typically several orders of magnitude smaller and are commonly neglected in practical turbulence modeling. Following this standard practice, we evaluate the error only on

$$\Omega = \{(0, 0), (0, 1), (1, 1), (2, 2)\}, \quad (18)$$

$$\text{MSE} = \frac{1}{|\Omega|} \sum_{(i,j) \in \Omega} \frac{1}{N} \sum_{n=1}^N \left( \tau_{ij}(x_n) - \hat{\tau}_{ij}(x_n) \right)^2. \quad (19)$$

The resulting MSE is used as the numerical fitting score for the symbolic regression loop.

*Prompt and fairness across methods.* We provide the same problem specification text (task description, variable definitions, and operator constraints) to both LLM-SR and PrT-PO to ensure a fair comparison. An example prompt is shown in Figure 11–13. In our current experiments, we also explicitly restrict the hypothesis space by asking the LLM to avoid trigonometric functions.

```
"""
Task: Symbolic regression for periodic hill turbulence modeling.
Learn three scalar functions G1(I1, I2), G2(I1, I2), G3(I1, I2).

[Flow case context (for description only)]
- Bottom wall profile:
  y(x) = a[1 + cos(π x / L)] for |x| ≤ L
  y(x) = 0 for |x| > L
  where a is the hill height (characteristic length h), and a = L/h controls hill steepness (training case: a = 0.8).
- Streamwise (x) direction uses periodic boundary conditions; top and bottom walls use no-slip boundary conditions.
- Reynolds number: Re_h = U_h h / v = 5600.

[Evaluation rule]
Given tensor bases T1, T2, T3 (each 3x3), the predicted anisotropy is:
  b_hat = G1 * T1 + G2 * T2 + G3 * T3

The evaluator computes MSE between b_hat and the target b.

[Tensor bases: T1, T2, T3 (provided by the evaluator, do NOT compute them)]
For each sample n, the evaluator provides three 3x3 tensor bases (symmetric, traceless) constructed from the non-dimensionalized mean strain-rate tensor S and rotation tensor R:
  - T1 (linear strain basis):
    T1 = S
    Interpretation: the Boussinesq/linear eddy-viscosity direction. It dominates in simple shear flows and acts as the baseline anisotropy response aligned with the mean strain.
  - T2 (strain-rotation coupling basis):
    T2 = S @ R - R @ S
    Interpretation: captures the interaction between mean strain and mean rotation (curvature/turning, strong vortices). This term is crucial in separated flows, reattachment, and swirling/shear-layer regions where linear eddy-viscosity assumptions tend to fail.
  - T3 (quadratic strain nonlinearity basis):
    T3 = S @ S - (1/3) * tr(S @ S) * I
    Interpretation: introduces nonlinear strain effects and normal-stress anisotropy beyond linear models. It helps represent differences among normal stress components and improves predictions in strongly anisotropic regions.

The predicted anisotropy is assembled as:
  b_hat = G1(I1, I2) * T1 + G2(I1, I2) * T2 + G3(I1, I2) * T3
"""

```

Figure 11: Problem Specification.

### E.3 Back to Turbulence Modeling

*From discovered expressions to a deployable closure.* After obtaining an explicit expression for the Reynolds-stress-related term from symbolic regression, we rewrite the discovered formula into an OpenFOAM-readable form.

*Embedding into OpenFOAM.* We embed the resulting closure into the existing kOmegaSST implementation by replacing the routine that evaluates the Reynolds stress (or its modeled contribution) with the discovered expression, thereby forming an optimized turbulence model within the RANS framework.

*Verification against DNS.* We then run RANS simulations with the modified model under the same configuration as the baseline and compare the resulting flow statistics against the DNS reference data. This completes the end-to-end turbulence modeling and validation pipeline considered in this work.

```
def evaluate(data, equation):
    I1, I2 = data['inputs']
    T1, T2, T3 = data['tensors']
    b_true = data['outputs']

    # Define Loss Function
    def loss(params):
        # Predict scalar coefficients G = [G1, G2, G3]
        # equation returns shape (N, 3) based on params
        G_pred = equation(I1, I2, params)

        # Reconstruct predicted anisotropy tensor:
        # b_hat = G1*T1 + G2*T2 + G3*T3
        b_hat = (G_pred[:, 0, None, None] * T1 +
                 G_pred[:, 1, None, None] * T2 +
                 G_pred[:, 2, None, None] * T3)

        # Compute MSE against target
        return np.mean((b_hat - b_true) ** 2)

    # Initialize parameters (e.g., 30 params for the 3 scalar functions)
    initial_params = np.ones(30)
    result = minimize(loss, initial_params, method='BFGS')
    return result.fun
```

Figure 12: Evaluation and Optimization.

```
def equation(I1: np.ndarray, I2: np.ndarray, params: np.ndarray)
-> np.ndarray:
    """
    Predict three scalar coefficients G1, G2, G3 for tensor bases.
    Args:
        I1, I2: numpy arrays of shape (N,), invariants.
        params: numpy array of free constants.
    Returns:
        numpy array of shape (N, 3), columns are G1, G2, G3.
    """
    # G1 block: params[0:10]
    g1 = (
        params[0] * I1 +
        params[1] * I2 +
        params[2]
    )

    # G2 block: params[10:20]
    g2 = (
        params[10] * I1 +
        params[11] * I2 +
        params[12]
    )

    # G3 block: params[20:30]
    g3 = (
        params[20] * I1 +
        params[21] * I2 +
        params[22]
    )

    return np.stack([g1, g2, g3], axis=1)
```

Figure 13: Equation Program Example.

### E.4 Domain-Specific Constraints for Turbulence Modeling

To encode expert knowledge as inductive biases, we augment the reward with a domain-specific penalty term:

$$P_{\text{domain}} = \sum_{j=1}^4 w_j P_{\text{domain}}^{(j)}, \quad (20)$$

where each  $P_{\text{domain}}^{(j)} \geq 0$  quantifies violations of the  $j$ -th turbulence constraint.

(1) *Realizability*. A physically admissible Reynolds stress tensor must be symmetric and positive semi-definite (PSD), which implies that all eigenvalues are nonnegative. Non-realizable predictions are penalized by

$$P_{\text{domain}}^{(1)} = \frac{1}{N} \sum_{n=1}^N \max\left(0, -\lambda_{\min}(\tau(x_n))\right), \quad (21)$$

where  $\lambda_{\min}(\cdot)$  denotes the smallest eigenvalue. This PSD requirement is a standard realizability condition for Reynolds stresses [32].

(2) *Boundary-condition consistency*. At a no-slip wall, the Reynolds stress tensor must decay to zero. Accordingly, non-vanishing stresses in a near-wall band  $\mathcal{W} = \{x : y(x) < y_0\}$  are penalized as

$$P_{\text{domain}}^{(2)} = \frac{1}{|\mathcal{W}|} \sum_{x_n \in \mathcal{W}} \|\tau(x_n)\|_F, \quad (22)$$

where  $y(x)$  is the wall distance field. In practice,  $y(x)$  can be computed and exported using standard CFD post-processing tools (OpenFOAM wall-distance utilities such as `wallDist` and `checkMesh-writeAllFields`) [27].

(3) *Asymptotic scaling in the viscous sublayer*. Near-wall Taylor expansions under the no-slip constraint imply that  $u' = O(y)$  and, for incompressible flow,  $v' = O(y^2)$ . Consequently, the Reynolds shear stress  $-u'v'$  exhibits cubic leading-order scaling,  $O(y^3)$ , in the viscous sublayer [44]. This constraint is enforced by evaluating the slope of  $\log|\tau_{xy}^+|$  with respect to  $\log(y^+)$  over the viscous sublayer range  $\mathcal{V} = \{x : y^+(x) \in [y_1^+, y_2^+]\}$ :

$$p = \text{slope}(\log|\tau_{xy}^+| \text{ vs } \log(y^+)), \quad P_{\text{domain}}^{(3)} = |p - 3|. \quad (23)$$

Here  $y^+ = y u_\tau / v$  is the wall unit, with friction velocity  $u_\tau = \sqrt{\tau_w / \rho}$ . In CFD,  $y^+$  and  $\tau_w$  can be obtained through standard post-processing utilities (OpenFOAM `yPlus` and `wallShearStress`).

(4) *Energy consistency*. Energy consistency is enforced by constraining the turbulent kinetic energy production implied by the predicted stress:

$$P_k(x) = -\tau_{ij}(x) \frac{\partial U_i}{\partial x_j}(x), \quad (24)$$

and penalizing mismatches with the reference production  $P_k^{\text{ref}}$  (computed from DNS-aligned fields) via

$$P_{\text{domain}}^{(4)} = \text{MSE}(P_k, P_k^{\text{ref}}). \quad (25)$$

The definition in Eq. (24) is the standard production term in the TKE budget [32].

*Efficient evaluation via elite-CFD refinement (multi-fidelity constraint scheduling)*. Constraints (2)–(4) require additional CFD-derived fields (wall distance  $y$ , wall shear stress  $\tau_w$  and the associated  $y^+$ , and mean velocity gradients  $\nabla U$ ), which can be expensive to obtain at each candidate-evaluation step. To keep the symbolic regression loop efficient, we adopt a two-stage evaluation schedule.

**Stage-A (inexpensive screening, applied to all candidates)** evaluates the data-fitting score (MSE) together with realizability  $P_{\text{domain}}^{(1)}$  using only the predicted stress tensor.

**Stage-B (expensive physics checks, triggered by an improving best MSE)** is activated when a candidate in the current batch achieves a new best MSE value relative to all previously evaluated candidates. In this case, the candidate is treated as an elite solution, and CFD-based post-processing is performed to obtain the required auxiliary fields, compute  $P_{\text{domain}}^{(2)} - P_{\text{domain}}^{(4)}$ , and conduct an additional online fine-tuning step using the full domain-specific penalty. All non-elite candidates are trained only with the realizability constraint, whereas elite candidates receive the full turbulence constraint suite after CFD evaluation. This design enables rigorous physics enforcement without incurring prohibitive CFD costs during exploration.